

## THE PHYSICAL NATURE OF REST-UV GALAXY MORPHOLOGY DURING THE PEAK EPOCH OF GALAXY FORMATION

DAVID R. LAW,<sup>1</sup> CHARLES C. STEIDEL,<sup>1</sup> DAWN K. ERB,<sup>2</sup> MAX PETTINI,<sup>3</sup> NAVEEN A. REDDY,<sup>1</sup>  
ALICE E. SHAPLEY,<sup>4</sup> KURT L. ADELBERGER,<sup>5</sup> AND DAVID J. SIMENC<sup>1</sup>

Received 2006 August 8; accepted 2006 October 22

### ABSTRACT

Motivated by the irregular and little-understood morphologies of  $z \sim 2-3$  galaxies, we use nonparametric coefficients to quantify the morphologies of 216 galaxies that have been spectroscopically confirmed to lie at redshifts  $z = 1.8-3.4$  in the GOODS-N field. Using measurements of UV and optical spectral lines, multiband photometric data, and stellar population models, we statistically assess possible correlations between galaxy morphology and physical observables such as stellar mass, star formation rate, and the strength of galaxy-scale outflows. We find evidence that dustier galaxies have more nebulous UV morphologies and that larger, more luminous galaxies may drive stronger outflows, but we otherwise conclude that UV morphology is either statistically decoupled from the majority of physical observables or determined by too complex a combination of physical processes to provide characterizations with predictive power. Given the absence of strong correlations between UV morphology and physical parameters such as star formation rates, we are therefore unable to support the hypothesis that morphologically irregular galaxies predominantly represent major galaxy mergers. Comparing galaxy samples, we find that IR-selected *BzK* galaxies and radio-selected submillimeter galaxies have UV morphologies similar to the optically selected sample, while distant red galaxies are more nebulous.

*Subject headings:* cosmology: observations — galaxies: fundamental parameters — galaxies: high-redshift — galaxies: irregular — galaxies: starburst — galaxies: structure

### 1. INTRODUCTION

In the local universe the projected distribution of luminous matter within a galaxy, i.e., the morphology, often provides a wealth of information about that galaxy's kinematics, rate of star formation, and recent merger history. In the classical picture, late-type spiral galaxies harbor active star formation in the gas-rich arms of a flattened rotating disk, while early-type elliptical galaxies tend to be more massive, dispersion-supported, and quiescent systems. At high redshifts  $z \sim 2-3$ , however, the morphologies of typical galaxies are highly irregular (Abraham et al. 1996; Kajisawa & Yamada 2001; Conselice et al. 2005), frequently composed of multiple spatially separated components, and appear to bear little similarity to the local Hubble-type population. It is uncertain whether these irregular morphologies are due to patchy star formation, prevalent merger activity, or some other physical process and consequently unknown whether these morphologies can (analogously to local galaxies) tell us anything about the star formation rate (SFR), mass, or stellar kinematics of galaxies at high redshifts.

Since morphological studies are often performed at optical wavelengths that probe rest-frame ultraviolet (UV) radiation for galaxies at redshifts  $z \gtrsim 1$ , one might *expect* that the morphologies of such galaxies should appear irregular since radiation at such wavelengths predominantly traces emission from the brightest active star-forming regions rather than the redder bulk of the stellar population (Dickinson 2000). UV emission tends to be patchy and

irregular even for local Hubble-type galaxies (e.g., Gordon et al. 2004), as in the case of the local galaxy merger VV 114 (whose broad rest-UV absorption-line spectra suggest that it may be a local analog to  $z \sim 2-3$  Lyman break galaxies [LBGs]; Grimes et al. 2006), whose near-infrared (NIR) morphology clearly shows a pair of interacting late-type galaxies while the rest-UV morphology shows only scattered clumps of emission (Goldader et al. 2002). However, high-redshift galaxies have irregular morphologies not only in the rest-UV, but often at rest-optical wavelengths as well (Dickinson 2000; Papovich et al. 2005), indicating that (in contrast to local galaxies) both wavelength regimes are dominated by emission from young starbursting components and therefore that there may be some fundamental difference between the two samples.

One popular explanation for these multicomponent, irregular morphologies is that they represent major merger systems and that their prevalence indicates that the rate of major mergers was much greater at high redshifts than in the local universe (e.g., Conselice et al. 2003a). Such a conclusion fits well within the framework of cold dark matter (CDM) theory and may additionally be supported by stellar population analyses (e.g., Dickinson et al. 2003), which suggest that many galaxies in the local universe accumulated a large fraction of their stellar mass at  $z \sim 2-3$  as might be expected if star formation peaked in this epoch as a result of tidally induced collapse spurred by major mergers. However, the interpretation of a multicomponent or otherwise irregular morphology is not always clear. In the case of VV 114, NIR imaging (Goldader et al. 2002) indicates that all of the clumps of UV emission are associated with only one galaxy of the merger pair and that the multicomponent UV morphology therefore directly reflects clumpy star formation rather than tracing tidally distorted features from each of the two galaxies.

Building on a body of literature characterizing the morphologies of galaxies at redshifts  $z \sim 2-3$  (e.g., Abraham et al. 2003;

<sup>1</sup> Department of Astronomy, California Institute of Technology, Pasadena, CA; drlaw@astro.caltech.edu, ccs@astro.caltech.edu, nar@astro.caltech.edu, dsimenc@caltech.edu.

<sup>2</sup> Harvard-Smithsonian Center for Astrophysics, Cambridge, MA; derb@cfa.harvard.edu.

<sup>3</sup> Institute of Astronomy, Cambridge, UK; pettini@ast.cam.ac.uk.

<sup>4</sup> Department of Astrophysical Sciences, Princeton University, Princeton, NJ; aes@astro.princeton.edu.

<sup>5</sup> McKinsey and Company, Seattle, WA; kurt@ociw.edu.

Conselice et al. 2003a; Lotz et al. 2004, hereafter LPM04; Lotz et al. 2006; Ravindranath et al. 2006), it is worthwhile to ask whether rest-UV morphologies correspond to any other physical observables such as UV/optical spectral line strengths (e.g., Shapley et al. 2003; Erb et al. 2006a), stellar population models (e.g., Shapley et al. 2005; Erb et al. 2006a; Reddy et al. 2006a), or rest-optical to IR properties (e.g., Reddy et al. 2006a, 2006b). In this work we use nonparametric coefficients to characterize the morphologies of 216 spectroscopically confirmed galaxies in the redshift range  $z = 1.8\text{--}3.4$ , assess the statistical significance of correlations with spectrophotometric observables, and discuss the resulting physical interpretation of galaxy morphology. In § 2 we describe our galaxy sample and give a basic description of the sample population. In § 3 we outline our morphological parameters, comparing our results to the recent studies of Conselice et al. (2003a), LPM04, and Lotz et al. (2006). Rest-frame UV spectra are introduced in § 4, and correlations between morphology and spectral line strength and kinematics are discussed in § 5. In §§ 6 and 7 we compare morphologies with stellar population models derived from UV to mid-IR photometric data, as well as discussing differences between different samples of high-redshift galaxies and active galactic nuclei (AGNs) selected on the basis of various photometric criteria. Finally, we discuss the implications of our results for the physical interpretation of galaxy morphologies in § 8. Our morphological statistics and ancillary data are made publicly available in an electronic database.<sup>6</sup>

We assume a standard  $\Lambda$ CDM cosmology in which  $H_0 = 71 \text{ km s}^{-1} \text{ Mpc}^{-1}$ ,  $\Omega_m = 0.27$ , and  $\Omega_\Lambda = 0.73$ .

## 2. SAMPLE SELECTION

Our sample is drawn from rest-UV color-selected catalogs of  $z \sim 2\text{--}3$  star-forming galaxy candidates (Steidel et al. 2003, 2004; Adelberger et al. 2004) in the GOODS-N field. These catalogs are based on deep ground-based imaging and therefore select galaxies independent of morphology or surface brightness since even the largest galaxies are nearly unresolved in these seeing-limited images. We consider only those galaxies that have been spectroscopically confirmed to lie in the redshift intervals  $z = 1.8\text{--}2.6$  or  $z = 2.6\text{--}3.4$  (i.e., the peak redshift ranges defined by the selection functions of the color selection criteria; see Adelberger et al. 2004) and that exhibit no obvious spectroscopic signatures of AGNs.

The redshift distribution of galaxies in our sample is shown in Figure 1: the  $z \sim 2$  sample contains 150 galaxies in the range  $1.8 < z < 2.6$  with mean  $\bar{z} = 2.17 \pm 0.21$ , while the  $z \sim 3$  sample contains 66 galaxies in the range  $2.6 < z < 3.4$  with  $\bar{z} = 3.02 \pm 0.19$ .

## 3. MORPHOLOGIES

Morphological parameters were determined from deep *Hubble Space Telescope* (*HST*) Advanced Camera for Surveys (ACS) imaging obtained as part of the GOODS-N survey (Giavalisco et al. 2004) in F435W (*B*), F606W (*V*), F775W (*I*), and F850LP (*z*) bandpasses with drizzled pixel scale of  $50 \text{ mas pixel}^{-1}$  and  $10 \sigma$  limiting point-source sensitivities of 27.8, 27.8, 27.1, and 26.6 mag (AB), respectively (Giavalisco et al. 2004). At redshifts  $z \sim 2$  and  $z \sim 3$  these bandpasses collectively probe rest-frame UV emission in the wavelength intervals  $\sim 1500\text{--}3000 \text{ \AA}$  and  $\sim 1000\text{--}2000 \text{ \AA}$ , respectively.

The observed morphology is qualitatively similar throughout this range of wavelengths (see § 3.6), and we therefore improve our signal-to-noise ratios per pixel by creating a single rest-frame UV image from a weighted sum of the four individual bandpasses.

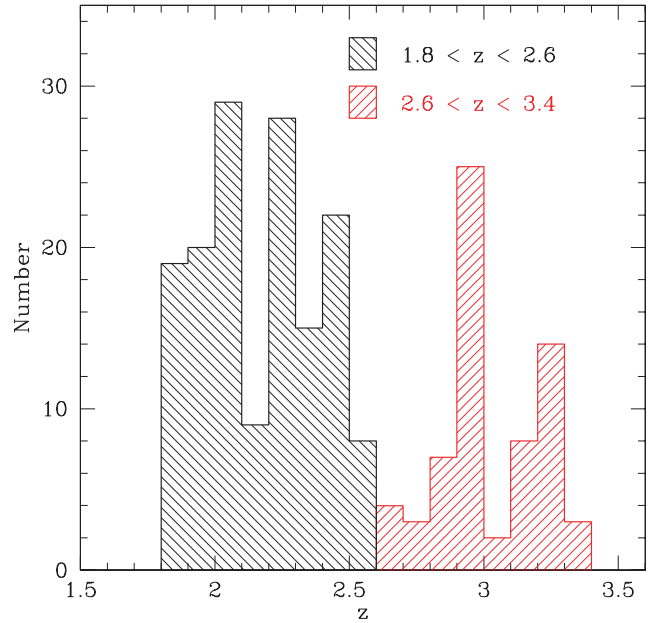


FIG. 1.—Distribution of galaxies with spectroscopic redshift  $z$  in the  $z \sim 2$  and  $z \sim 3$  galaxy samples.

Weights for this sum are determined proportionally to the inverse variance of the overall sky noise relative to the average number of counts from the  $z \sim 2\text{--}3$  galaxies. The UV composite morphologies of our 216 galaxies are shown in Figure 2 in order of increasing redshift and demonstrate a variety of morphological types ranging from single nucleated<sup>7</sup> sources to extremely asymmetric sources with multiple nucleations and/or nebulous components. The “typical” galaxy has a morphology comprising one or more spatially distinct clumps with some degree of diffuse nebulosity, reminiscent of the *HST* Space Telescope Imaging Spectrograph (STIS) UV morphology of the local interacting galaxy VV 114 (Goldader et al. 2002), which is dominated by a patchy distribution of star formation regions. Our initial morphological classification groups galaxies by visual inspection on the basis of the apparent nucleation of their light profiles and the presence and number of multiple nucleated emission components. Galaxies fall within five general classes:

1. Single strongly nucleated sources (11 sources at  $z \sim 2$ , nine sources at  $z \sim 3$ ).
2. Multiple strongly nucleated sources (six sources at  $z \sim 2$ , two sources at  $z \sim 3$ ).
3. Single nucleated source accompanied by nebulosity (61 sources at  $z \sim 2$ , 27 sources at  $z \sim 3$ ).
4. Multiple nucleated sources accompanied by nebulosity (35 sources at  $z \sim 2$ , 12 sources at  $z \sim 3$ ).
5. Nebulous emission with no strong nucleation (37 sources at  $z \sim 2$ , 16 sources at  $z \sim 3$ ).

We seek a set of numerical parameters that will allow us to effectively reproduce these intuitive divisions, while providing a more rigorous mathematical basis for the classification. The “CAS” system of parameters has recently been a popular choice, characterizing galaxies on the basis of their concentration ( $C$ ; Kent

<sup>7</sup> We adopt the term “nucleation” to qualitatively describe a concentrated region of flux that might naively be described as the “nucleus” of a given galaxy. This contrasts with the term “nebulosity,” which we use to describe diffuse flux that is spread fairly uniformly over a number of pixels.

<sup>6</sup> Available at <http://www.astro.caltech.edu/~drlaw/GOODS/>.

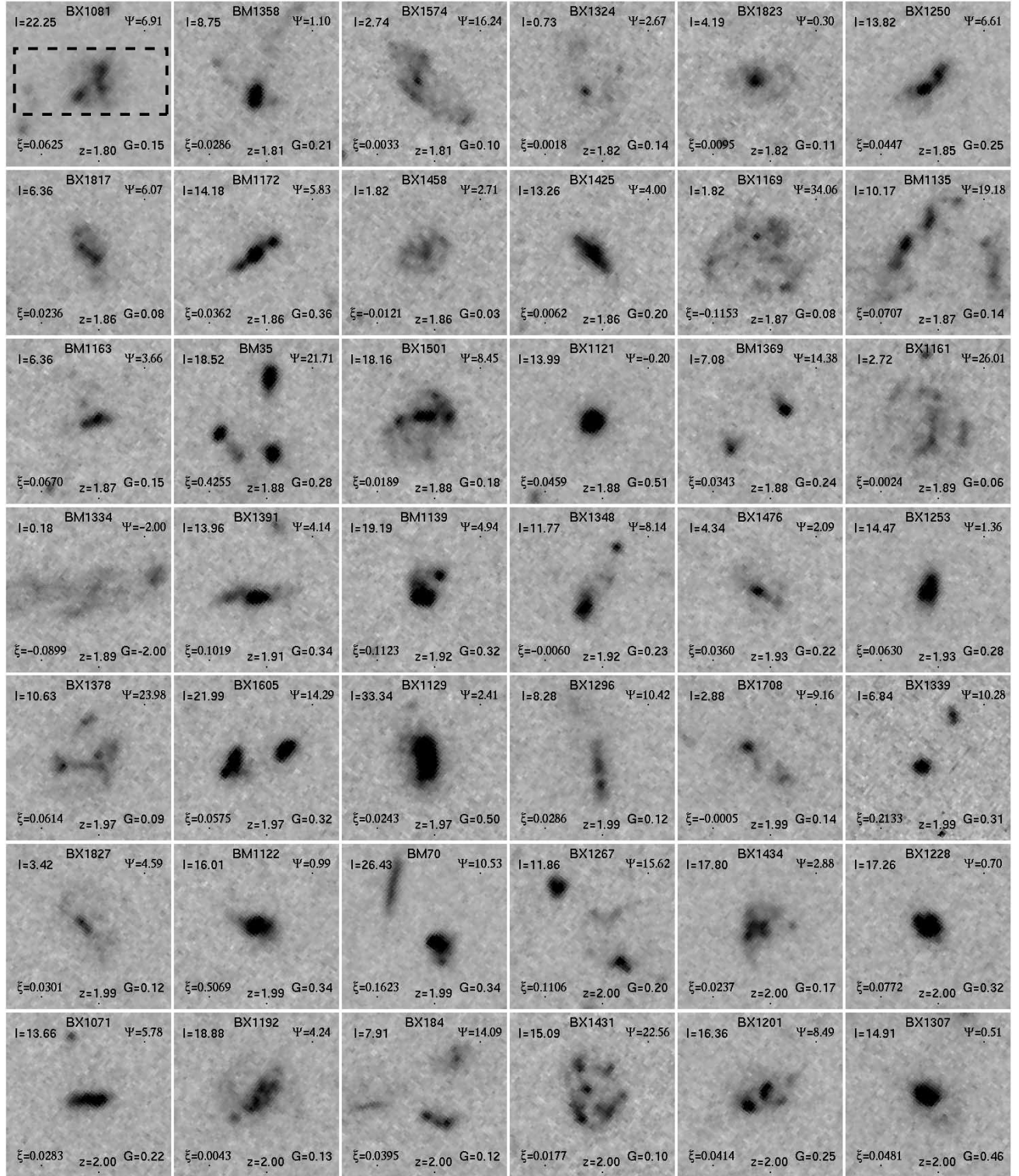


FIG. 2.—*HST* ACS rest-UV morphologies of the  $z \sim 2-3$  galaxy sample, sorted in order of increasing redshift. All panels include the galaxy name, redshift  $z$ , and morphological parameters size ( $l$ ), Gini ( $G$ ), multiplicity ( $\Psi$ ), and color dispersion ( $\xi$ ). Images are  $3''$  on a side, oriented with north up and east to the left. Values of  $-2.00$  for a particular morphological parameter indicate that a galaxy had too few pixels of suitably high surface brightness to define the parameter. Gray scale is logarithmic and chosen to emphasize the visibility of fainter nebulous regions; the details of high surface brightness features are thus suppressed. The  $1.2''$  width of the LRIS slit is indicated by a dashed box in the top left panel.

1985; Bershadsky et al. 2000), asymmetry ( $A$ ; Schade et al. 1995), and clumpiness ( $S$ ; Conselice 2003). However, the first two of these quantities are explicitly defined with regard to circular or elliptical apertures measured about a central point, which is only well defined for galaxies with morphologies similar to traditional

elliptical or spiral galaxies, while the third quantity relies on the suitable choice of a smoothing scale on which clumpiness is defined. In the case of the  $z \sim 2-3$  galaxy sample, morphologies are generally so irregular (see Fig. 2) that they do not have a well-defined “center,” and the measured values of the *CAS* parameters

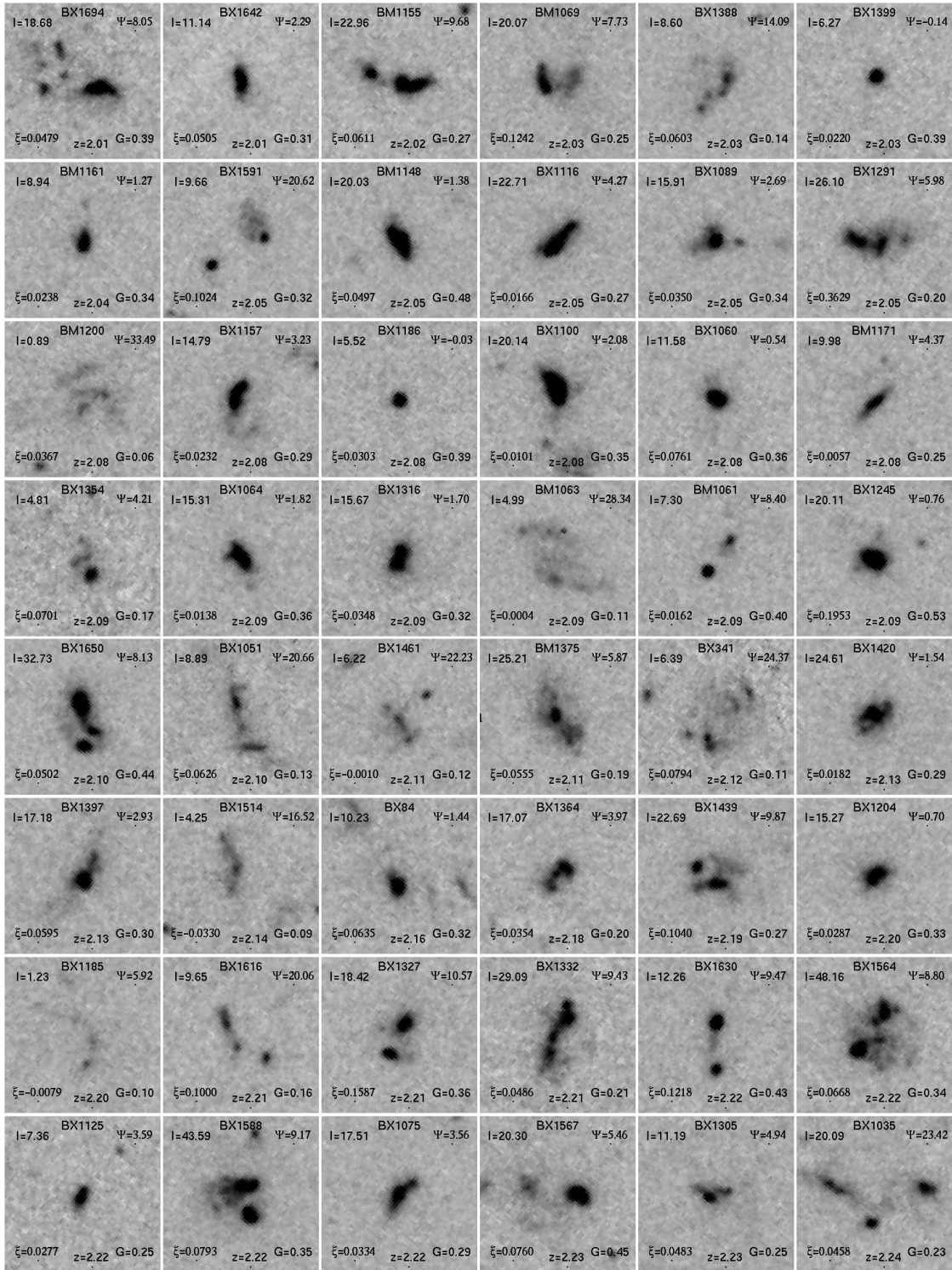


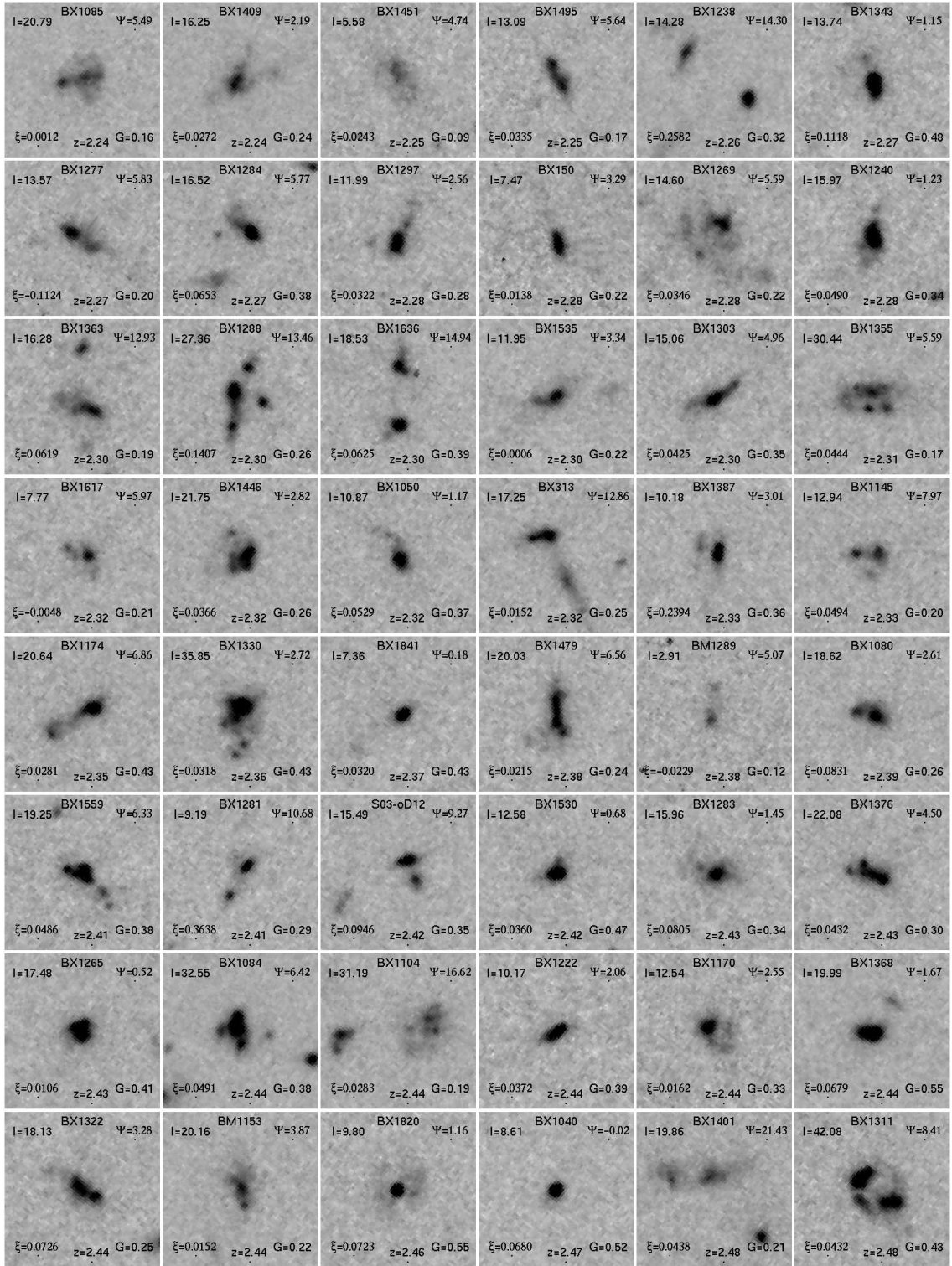
FIG. 2.—Continued

can depend strongly on the particular choice of center<sup>8</sup> and smoothing length (for a detailed discussion see LPM04).

We therefore favor a nonparametric approach to classification similar to that discussed by Abraham et al. (2003), LPM04,

<sup>8</sup> The asymmetry parameter  $A$  is strictly found by numerically searching through the image for the choice of center that minimizes the value of  $A$  (see discussion by Conselice et al. 2000). While this relaxation technique partially mitigates bias arising from poor centering, it does not address the underlying bias present in the assumption of circular symmetry for galaxies as irregular as those depicted in Fig. 2.

and Lotz et al. (2006), who define the Gini coefficient  $G$  as a measure of the uniformity of the flux distribution within a source. In the following sections we describe this and three additional nonparametric coefficients that we find effectively characterize the irregular morphologies of these  $z \sim 2-3$  galaxies. We note that although we considered a host of additional parameters in our analyses (including the Petrosian radius and a nonparametric “Petrosian area”), we found that they provided no additional information and therefore omit them from further discussion.

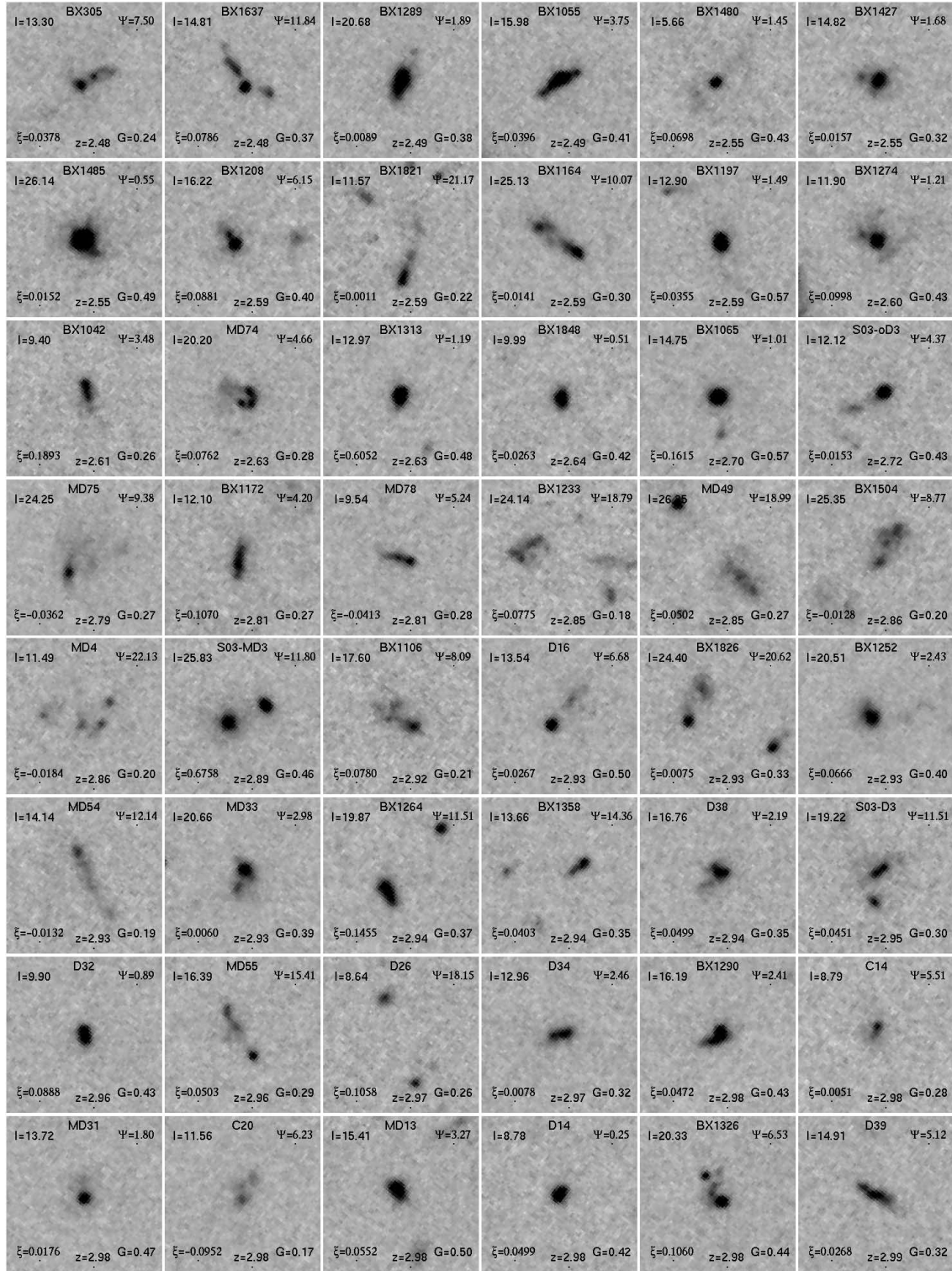
FIG. 2.— *Continued*

### 3.1. Pixel Selection

It is of critical importance when measuring the morphologies of faint and highly irregular galaxies to apply uniform selection criteria by which to assign pixels to a galaxy as opposed to the surrounding sky (i.e., defining the “segmentation map” of the source). A variety of criteria have been adopted in previous studies, ranging from complex methods based on curve-of-growth

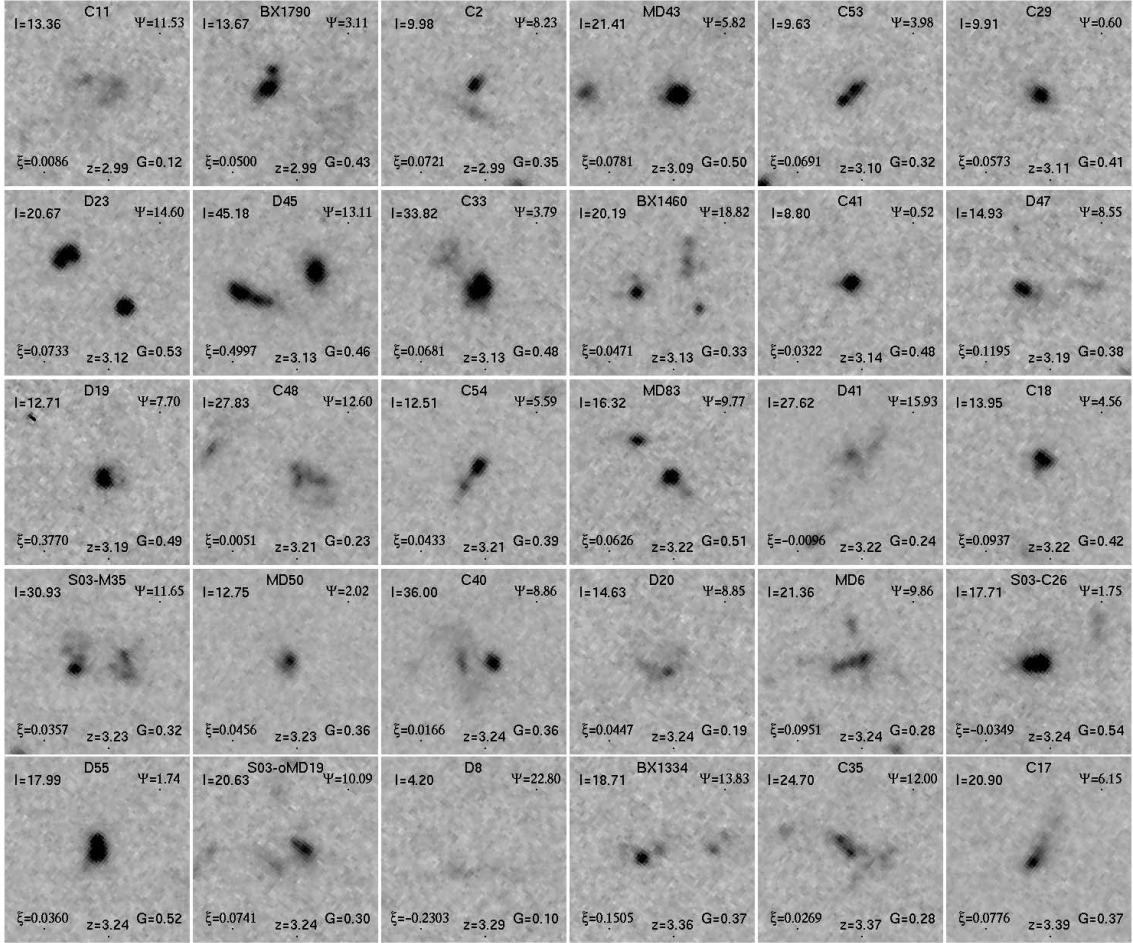
analysis (e.g., LPM04) to basic surface brightness selection (e.g., Abraham et al. 2003).

The first of these methods, while robust to cosmological surface brightness dimming, can be nontrivial to implement in a manner consistent with nonparametric analysis. As outlined by LPM04, the curve-of-growth method calculates the elliptical Petrosian radius of a source (i.e., the radius from the center of the source at which the average flux falls to a fixed fraction of the total inscribed

FIG. 2.— *Continued*

flux; Petrosian 1976) and assigns to the segmentation map all pixels within a suitably large radius of this center whose fluxes are greater than the value at the Petrosian radius. Unfortunately, such a segmentation map enforces elliptical Petrosian radii about a particular center and introduces biases similar to that of the *CAS* system into the resulting morphological coefficients. While such a segmentation map is useful for sources with approximately ellip-

tical isophotes, we find that it tends to fail for galaxies with multiple components or extremely irregular shapes since pixels at a particular “Petrosian” radius from an artificial center tend to include a large number of sky pixels, decreasing the threshold for surface brightness selection and resulting in some fraction of sky pixels being allocated to the galaxy in the final segmentation map. While the most noticeable cases may be fixed by hand, this

FIG. 2.— *Continued*

nonetheless introduces a bias as a function of morphological irregularity. We explore the effect of this bias on the measured Gini coefficient in further detail in § 3.3.

In contrast, the second of these methods (basic surface brightness selection) takes no account of surface brightness dimming but is more amenable to nonparametric analysis. However, with the aid of our confirmed spectroscopic redshifts for each galaxy in the optically selected sample, we adapt this morphology-independent surface brightness selection technique to utilize a variable threshold tuned to select pixels in an identical range of intrinsic surface brightnesses at each redshift.

Our segmentation map is calculated as follows: For each galaxy, we use our initial estimates of the position (based on seeing-limited  $U_nGR$  imaging) to calculate the first-order moment of the *HST* ACS UV flux distribution within a  $1.5''$  (30 pixel) radius. A revised value for the center is calculated using this first-order moment, and all pixels within a  $1.5''$  radius (i.e., slightly larger than the size of the largest galaxy in our sample, so the exact position of the “center” is unimportant) of this new center are considered as possible candidates for assignment to the segmentation map. While the ACS data product images have already been sky subtracted, we find that this subtraction is sometimes imperfect and therefore subtract off residual sky flux measured in an annulus of radius  $1.5''$ – $2''$  around the revised center (using a  $3\sigma$  rejection algorithm to eliminate possible contaminating flux from sources that are nearby in projection). Generally, these residual sky fluxes were small compared to the calculated object flux.

Once this preprocessing is complete, we assign to the segmentation map all pixels whose flux is at least  $n\sigma$ , where  $\sigma$  is the standard deviation of pixel values in the sky annulus, and where  $n$  varies with redshift as

$$n = 3 \left( \frac{1+z}{1+z_{\max}} \right)^{-3}. \quad (1)$$

This variable surface brightness selection compensates for the effects of cosmological dimming throughout our range of sample redshifts since (for a fixed observed bandpass) surface brightness scales as  $(1+z)^{-3}$  and our selection criteria therefore include pixels of the same intrinsic surface brightness at all redshifts (we make the assumption that there is no intrinsic evolution of surface brightness with redshift, although see discussion in § 3.2). We set  $z_{\max} = 3.4$  (i.e., the upper end of our redshift distribution), so the value of the selection threshold varies by a factor of about 4 across our redshift interval from  $3\sigma$  at redshift  $z = 3.4$  to  $\sim 12\sigma$  at  $z = 1.8$ . We neglect the change in angular size with redshift since the angular diameter distance changes by only  $\sim 13\%$  over  $z \sim 1.8$ – $3.4$  for our assumed cosmology. The physical interpretation of our adopted segmentation map is illustrated in Figure 3, which shows the pixels selected for a typical source according to 3, 5, and 10  $\sigma$  criteria.

We note that by considering only flux within a  $1.5''$  radius we effectively restrict our sensitivity to morphology on distance scales  $\lesssim 13$  kpc at the redshift of our sample, similar to previous

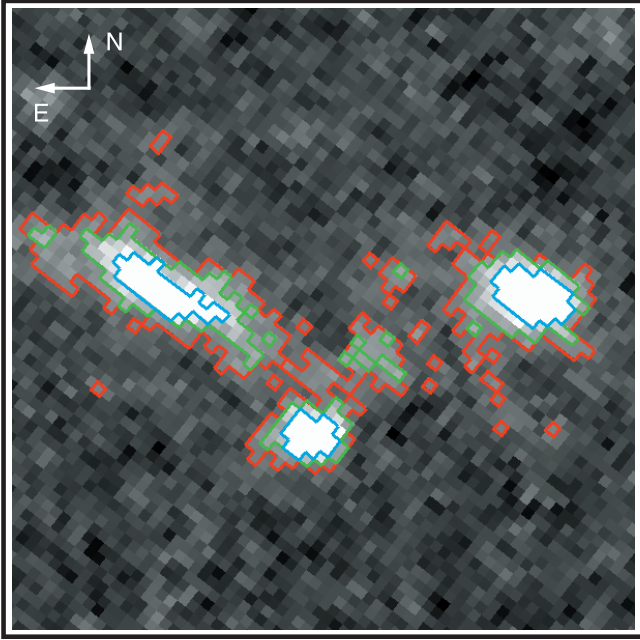


FIG. 3.—Stacked ACS rest-UV image of BX 1035 ( $z = 2.238$ ), overlotted with outlines of the 3, 5, and 10  $\sigma$  segmentation maps (red, green, and cyan outlines, respectively). The gray scale is linear in flux with the white point set to 10  $\sigma$ ; the field of view is  $3'' \times 3''$  (corresponding to a physical region  $25 \times 25$  kpc at the redshift of the source).

analyses (Conselice et al. 2003a; LPM04; Lotz et al. 2006) whose selection radii range up to about 10 kpc. Based on visual analysis of ACS and ground-based color maps, this appears to be the optimal choice of distance scale to include the majority of likely components for a particular galaxy while almost entirely excluding probable contaminants that appear nearby in projection. While it is likely that some gravitationally interacting systems extend considerably beyond 13 kpc, we neglect these distant components in our characterization of the system morphology since (1) our photometric and spectroscopic data are sensitive only to light at radii  $\lesssim 1.5''$  and (2) close interactions are more likely than distant ones to produce observable changes in the physical state of a galaxy.

### 3.2. The Size Parameter: $I$

The simplest morphological parameter to define is the projected physical size of the source ( $I$ ) seen above our surface brightness threshold (we use  $I$  instead of the more intuitive  $S$  to avoid confusion with the “clumpiness” parameter of Conselice 2003). Since the radius of a galaxy is not meaningful for multicomponent systems, we use our spectroscopic redshifts to define  $I$  as the total projected galaxy area in square physical kpc.<sup>9</sup> That is,

$$I = N(0.05'' \text{ pixel}^{-1})^2 (2.4 \times 10^{-11} \text{ sr arcsec}^{-2}) D_A^2, \quad (2)$$

where  $N$  is the total number of  $50 \text{ mas} \times 50 \text{ mas}$  pixels in the segmentation map and  $D_A$  is the angular diameter distance (in kpc) to redshift  $z$  for the assumed cosmology. This parameter makes no attempt to discriminate between sources on the basis of the total amount or relative distribution of flux within the segmentation map and may therefore classify similarly both small strongly nu-

cleated sources (which have a low number of high-flux pixels) and large yet extremely faint and nebulous sources (which have a low number of low-flux pixels barely satisfying the surface brightness selection criteria).

In Figure 4 we plot the distribution of  $I$  for the  $z \sim 2$  and  $z \sim 3$  samples (top left panel, black and red histograms respectively).  $I$  typically ranges in value from less than  $5 \text{ kpc}^2$  for faint and nebulous sources to around  $10 \text{ kpc}^2$  for the most strongly nucleated single sources, and up to as much as  $48 \text{ kpc}^2$  for the brightest extended sources. In the  $z \sim 2$  and  $z \sim 3$  samples the mean projected size is  $\bar{I} = 15.0 \pm 0.7$  and  $17.4 \pm 0.9 \text{ kpc}^2$ , respectively.<sup>10</sup> This small ( $\sim 3 \sigma$ ) apparent increase in average size from  $z \sim 2$  to  $z \sim 3$  arises because the  $z \sim 3$  sample does not extend as far down the luminosity function as the  $z \sim 2$  sample and small faint sources are therefore underrepresented in the  $z \sim 3$  sample. If we compare only the fraction of the  $z \sim 2$  sample that overlaps the  $z \sim 3$  sample in rest-frame UV luminosity ( $L_{1600} > 2 \times 10^{10} L_\odot$ ; Reddy et al. 2006a),<sup>11</sup> the average value of  $I$  at  $z \sim 2$  rises to  $\bar{I} = 16.7 \pm 1.0 \text{ kpc}^2$ , which is within  $1 \sigma$  of the  $z \sim 3$  result. Indeed, we note that in a recent analysis designed to more precisely measure the size evolution of galaxies (as determined from their SExtractor half-light radii) Ferguson et al. (2004) found that the angular size of single-component galaxies decreases with increasing redshift above  $z \sim 1$ .

### 3.3. The Gini Parameter: $G$

The Gini coefficient ( $G$ , originally attributed to Corrado Gini [Gini 1912] and first introduced into the astronomical literature by Abraham et al. 2003) measures the cumulative distribution function of a population and may be used to distinguish between the cases for which flux is strongly nucleated versus uniformly nebulous (for a detailed introduction see LPM04).

Mathematically,  $G$  may be calculated as (Glasser 1962)

$$G = \frac{1}{\bar{X}N(N-1)} \sum_{i=1}^N (2i - N - 1)X_i, \quad (3)$$

where  $\bar{X}$  is the average flux and the  $X_i$  pixel fluxes are sorted in increasing order before the summation over all  $N$  pixels in the segmentation map. The normalization prefactor multiplying the summation ensures that  $G$  takes values from zero to one inclusive, where low values indicate a uniform flux distribution and high values a concentration of flux in a few pixels.

Practically, we find that  $G$  differentiates clearly between galaxy morphologies based on the degree of nucleation of their UV emission: sources that appear very nebulous generally have  $G \lesssim 0.2$ , while sources with strongly nucleated emission have  $G \gtrsim 0.5$  (see Fig. 2). The wide range of galaxies with some combination of nucleated and nebulous emission components falls in a continuous distribution between these values. We note that this range of values ( $0 < G \lesssim 0.6$ ) is substantially different from that calculated for  $z \sim 2-4$  HDF-N LBGs by LPM04 and Lotz et al. (2006), who found  $0.4 < G < 0.7$ . While some discrepancy is to be expected with the LPM04 results since these authors used rest-optical data from *HST* NICMOS (although this difference should be minimal in light of the similarity between rest-UV and rest-optical morphologies), we should expect greater similarity to the findings of Lotz et al. (2006), who used *HST* ACS rest-UV

<sup>10</sup> Uncertainties quoted henceforth are uncertainties in the mean unless otherwise specified.

<sup>11</sup> A total of 62% of the  $z \sim 2$  sample members have well-determined measurements of  $L_{1600}$ , compared with 41% of the  $z \sim 3$  sample. A total of 84% of the  $z \sim 2$  sample members with measured  $L_{1600}$  have  $L_{1600} > 2 \times 10^{10} L_\odot$ .

<sup>9</sup> Given the small change in angular diameter distance across the redshift range of the sample, there is little practical difference between using physical and angular sizes in our analyses.

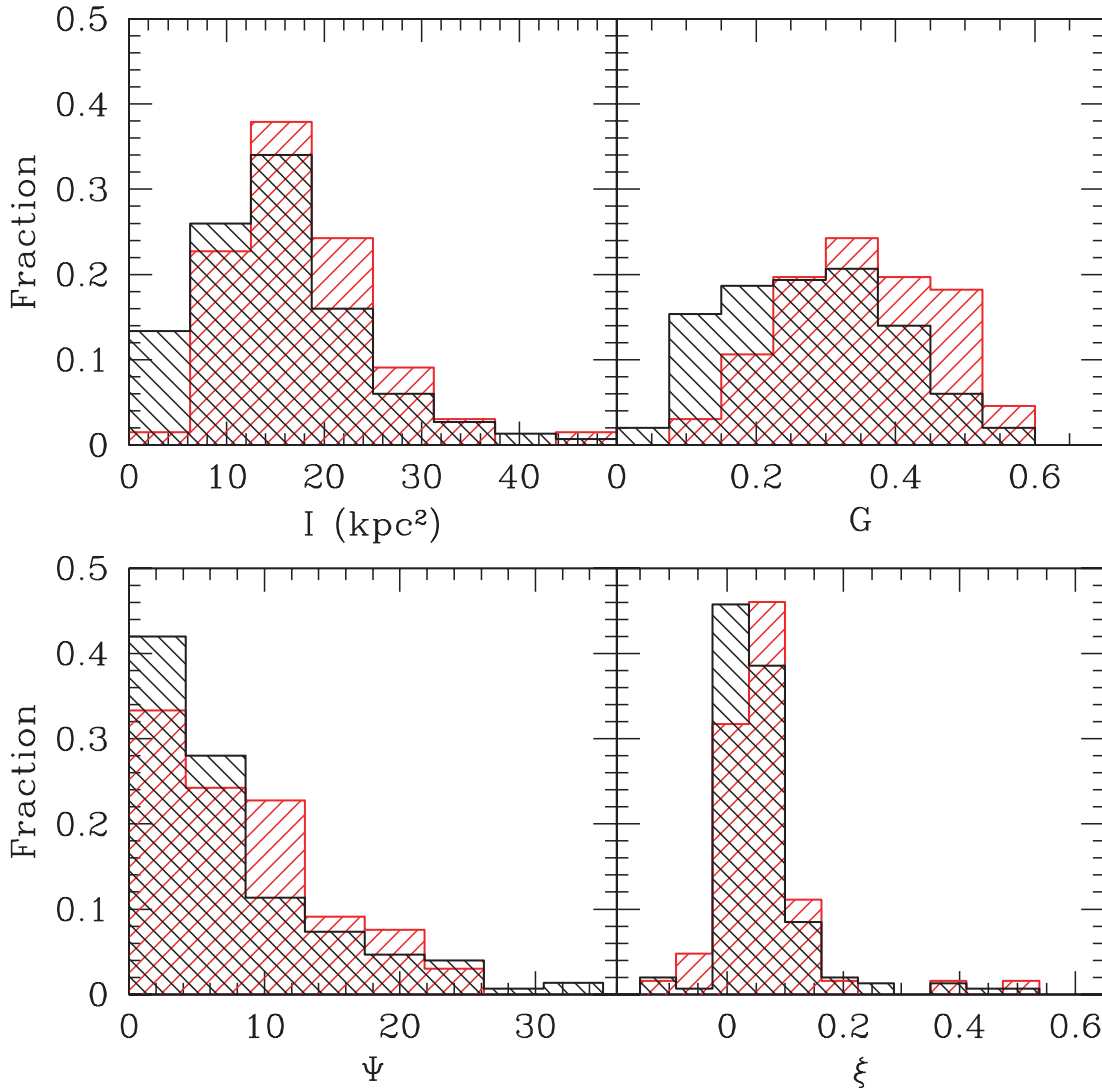


FIG. 4.—Relative distribution of the morphological parameters  $I$  (size),  $G$  (Gini),  $\Psi$  (multiplicity), and  $\xi$  (color dispersion) for the redshift  $z \sim 2$  and  $z \sim 3$  samples (black and red histograms, respectively). Counts are normalized by the total number of galaxies in each sample.

data similar to our own. This difference in results appears to arise primarily from the adopted pixel selection method; we find that elliptical Petrosian selection methods similar to those of LPM04 tend to include more sky pixels at the “Petrosian” radius for highly irregular and nebulous objects (i.e., low  $G$  in our sample), which lowers the threshold for assignment to the galaxy and includes more sky pixels in the resulting segmentation map. Including extra sky pixels in the map makes the genuine galaxy pixels appear to be comparatively more rich in flux, artificially increasing the value of  $G$  calculated for the sources. Applying a segmentation map similar to that of LPM04, we find that the Gini coefficient calculated for our highest  $G$  sources remains relatively unchanged, while our low Gini sources increase their values of  $G$  considerably, artificially compressing the range of values to  $0.4 \lesssim G \lesssim 0.6$ , closely mimicking the range of values presented by LPM04. We conclude that while the LPM04 values are accurate in the sense that a  $G = 0.4$  (in their calculation) galaxy is more nebulous than a  $G = 0.6$ , the noise introduced by this compression in dynamic range severely hampers the discriminating power of the Gini coefficient.

A histogram of values of  $G$  is plotted in Figure 4 and suggests that the mean value of the Gini coefficient appears to change from

$\bar{G} = 0.27 \pm 0.02$  at  $z \sim 2$  to  $\bar{G} = 0.35 \pm 0.01$  at  $z \sim 3$ . To some extent this may be due to the underrepresentation of faint, nebulous objects in the  $z \sim 3$  sample (see § 3.2), but even restricting the sample to the same range in intrinsic UV luminosity, the difference between the two samples is of order  $3 \sigma$ , suggesting that the UV emission from objects at  $z \sim 3$  is genuinely slightly more nucleated than at  $z \sim 2$ , consistent with the finding of Ferguson et al. (2004), who demonstrated that apparent galaxy size at constant luminosity decreases with increasing redshift.

We note that to first order,  $G$  does not distinguish between sources based on their number of nucleated components; i.e., a galaxy with two or more apparent nucleations has a value of  $G$  nearly identical to a galaxy with only one, so long as the cumulative distribution of light is similar. That is, the exact *spatial* distribution of flux is irrelevant to  $G$ , which is instead sensitive to the overall *curve of growth* of the total flux.

#### 3.4. The Multiplicity Parameter: $\Psi$

Our third classification parameter ( $\Psi$ ) is designed to discriminate between sources based on how many apparent components the light distribution is broken into, i.e., how “multiple” the source appears. This parameter is similar to both the asymmetry

parameter  $A$  (Schade et al. 1995) and the second-order moment of the 20% brightest pixels ( $M_{20}$ ; LPM04) in that it is sensitive to the presence and distribution of multiple clumps of flux. However, both  $A$  and  $M_{20}$  have their limitations:  $A$  depends strongly on the assumption of overall circular symmetry about some central point for each galaxy, while  $M_{20}$  is normalized by the moment of the segmentation map to remove the effect of overall galaxy size, which unfortunately results in a limited dynamic range since the segmentation map and the 20% brightest pixels often have a similar spatial distribution. In contrast,  $\Psi$  is defined in a manner that requires neither a center of symmetry nor a conventional normalization.

Using the observed flux distribution as a proxy for “mass,” we calculate the “potential energy” of the light distribution projected into our line of sight as

$$\psi_{\text{actual}} = \sum_{i=1}^N \sum_{j=1, j \neq i}^N \frac{X_i X_j}{r_{ij}}, \quad (4)$$

where the summation of the pixel fluxes  $X_i$  and  $X_j$  runs over all  $N$  pixels in the segmentation map and  $r_{ij}$  is the distance (in pixels) between pixels  $i$  and  $j$ . This value is normalized by that which would be achieved with the most compact possible rearrangement of the flux pixels, i.e., the configuration that would require the most “work” to pull apart. We rearrange the physical positions of the  $N$  pixels of the segmentation map in a circular configuration with the brightest pixel in the center and with pixel flux decreasing outward with radius. Calling the distance between pixels  $i$  and  $j$  in this rearranged map  $r'_{ij}$ , the projected potential energy of this compact light distribution is

$$\psi_{\text{compact}} = \sum_{i=1}^N \sum_{j=1, j \neq i}^N \frac{X_i X_j}{r'_{ij}}. \quad (5)$$

The multiplicity coefficient is then defined logarithmically as the ratio of these two quantities:

$$\Psi = 100 \log_{10} \left( \frac{\psi_{\text{compact}}}{\psi_{\text{actual}}} \right). \quad (6)$$

As shown in Figure 4,  $\Psi$  ranges from 0 up to about 30. Typically,  $\Psi = 0-2$  for single well-nucleated sources,  $\Psi \sim 5$  for sources that are beginning to show a second component in addition to the main nucleation, and  $\Psi \sim 10$  for strong double-nucleation systems. At values of  $\Psi > 10$ ,  $\Psi$  increases as the number and separation distance of nucleations increase, but numerical distinctions become less obvious until at  $\Psi \gtrsim 25$  the majority of sources are low- $G$  nebulous sources for which  $\Psi$  breaks down as a useful statistic (see § 3.6). There is therefore some degree of correlation between  $\Psi$  and the Gini coefficient  $G$  (Fig. 5) since sources with very nebulous emission (i.e., small  $G$ ) tend to have very spread out flux distributions (i.e., large  $\Psi$ ). However, this is of secondary importance to the largely orthogonal classification permitted by these two parameters; while  $G$  is most sensitive to the overall curve of growth of the flux distribution and fairly insensitive to the number of nucleated components,  $\Psi$  is sensitive to the number of bright components and comparatively insensitive to the overall curve of growth. We note that since  $\Psi$  is a flux-weighted statistic, it is more sensitive to bright pixels, and therefore a bright central source with an extremely faint secondary source will tend to have low  $\Psi$ , while the same

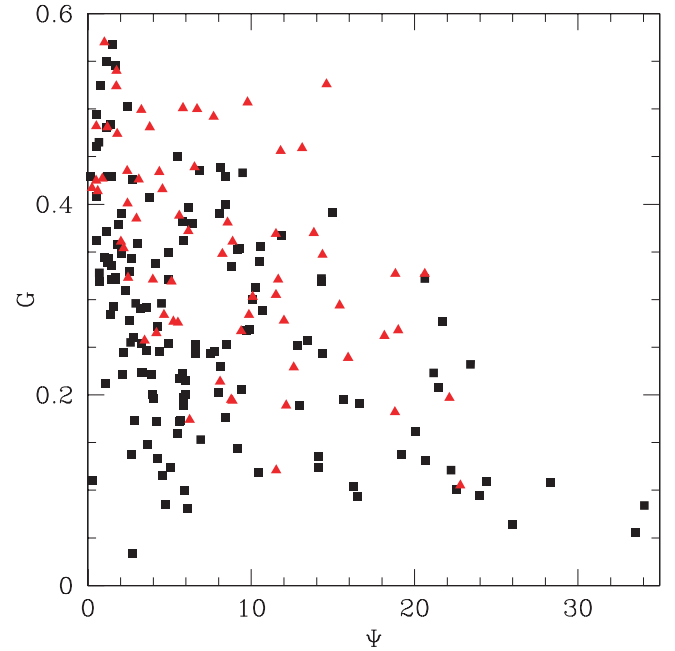


FIG. 5.—Distribution of  $G$  (Gini) vs.  $\Psi$  (multiplicity) for galaxies in the  $z \sim 2$  (black squares) and  $z \sim 3$  (red triangles) samples. Values are correlated in the sense that faint, nebulous galaxies tend to be broken into a greater number of noncontiguous components.

central source with a bright secondary source will tend to have higher  $\Psi$ .

### 3.5. The Color Dispersion: $\xi$

Finally, we capitalize on the available multiwavelength *HST* ACS data by defining the color dispersion parameter  $\xi$  (Papovich et al. 2003), which quantifies the degree of morphological difference between two bandpasses. Applied between rest-optical and UV wavelengths,  $\xi$  can measure the difference in spatial distribution between stellar populations of differing ages, convolved with variations in the dust distribution and resulting extinction (Papovich et al. 2003). Using rest-UV data alone,  $\xi$  is a less powerful statistic, but nevertheless potentially informative.

We calculate  $\xi$  as

$$\xi(I_V, I_z) = \frac{\sum(I_z - \alpha I_V - \beta)^2 - \sum(B_z - \alpha B_V)^2}{\sum(I_z - \beta)^2 - \sum(B_z - \alpha B_V)^2}, \quad (7)$$

where  $I_V, I_z$  are the object pixel fluxes in  $V$  and  $z$  bandpasses, respectively,<sup>12</sup>  $B_V, B_z$  are the background sky flux in the bandpasses,  $\alpha$  is the flux ratio between the two bands, and  $\beta$  represents the difference in background levels between the two bands. In brief, the first term in the numerator represents the summed square difference in pixel fluxes between the bands, the first term in the denominator represents the summed square total object flux (for normalization), and the second terms in both numerator and denominator represent corrections to statistically eliminate contributions to  $\xi$  from the natural background sky variance. Further details regarding the definition of this statistic are given by Papovich et al. (2003).

<sup>12</sup> While use of the  $B$  and  $z$  bands would provide a greater wavelength baseline for morphological differences, we use  $V$  instead since  $B$  is blanketed by absorption from the Ly $\alpha$  forest for galaxies in the upper end of our redshift range.

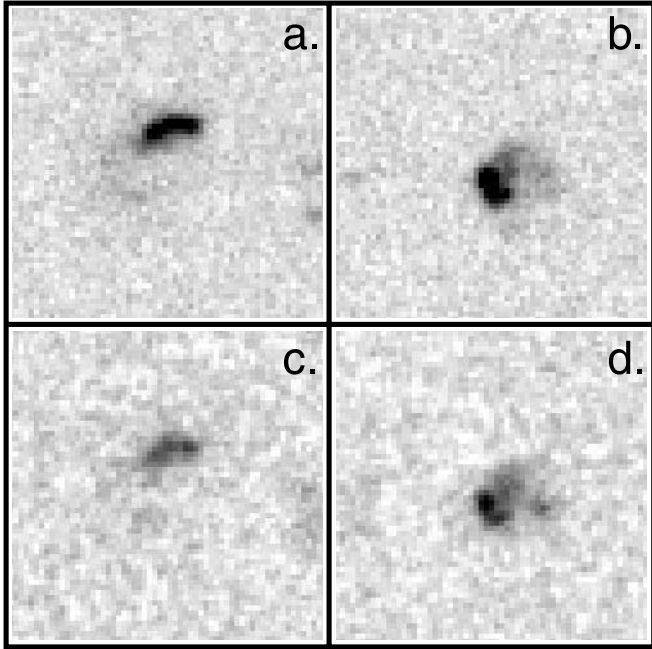


FIG. 6.—*HST* ACS images of BX 1157 and BM 1139 in F606W (panels [a] and [b], respectively) and in F850LP (panels [c] and [d]). Both galaxies have comparable redshifts ( $z = 2.08$  and  $1.92$ ), Gini ( $G = 0.291, 0.321$ ), and multiplicity ( $\Psi = 3.23, 4.94$ ) in the summed rest-UV image. Both galaxies show similar decrease in signal-to-noise ratio from F606W to F850LP but have widely variant color dispersions ( $\xi = 0.023, 0.112$ ). Image size and orientation are the same as in Fig. 2.

As shown in Figure 4, typical values range from  $\xi \sim 0.0$  to  $0.15$ , with  $\xi = 0.057 \pm 0.006$  at  $z \sim 2$  and  $\xi = 0.061 \pm 0.011$  at  $z \sim 3$  (i.e., consistent with a constant value to well within the uncertainty). We note that this range of values is larger than that of  $\xi \sim 0.0$ – $0.05$  found by Papovich et al. (2005) for a sample of  $z \sim 2.3$  galaxies measured between rest-UV and optical bandpasses. The origin of this discrepancy is uncertain, although it is likely that different galaxy samples, segmentation maps, and bandpasses all contribute. By and large, it appears that our calculated  $\xi$  is dominated mainly by scatter rather than by genuine differences between the apparent morphology in  $V$  and  $z$  bands. Figure 6 shows that for two galaxies with  $\xi = 0.023$  and  $0.112$  the most obvious trend from  $V$  to  $z$  bands is an overall decrease in the signal-to-noise ratio. Given the similarity of the effect in both cases, it is not readily apparent why the two galaxies should have such different color dispersions.

Curiously, while  $\xi$  has no obvious correlation with a visible difference in morphology between bands, it does correlate with the Gini coefficient  $G$  of a source (as shown in Fig. 7) in the sense that  $\xi$  is (on average) slightly larger in the most nucleated sources. This is likely a consequence of the flux weighting of  $\xi$ : high-flux pixels have greater absolute variation between bandpasses and tend to dominate the sum in equation (7), increasing  $\xi$  for high- $G$  sources where  $\xi$  is dominated by variation from a few bright pixels rather than averaging over a larger number of lower variation pixels for low- $G$  sources. In conclusion, we caution that while  $\xi$  is ideally a useful statistic, in the present case it may be too erratic to provide a great deal of information.

### 3.6. Robustness of the Parameters

We test the robustness of these parameters to cosmological distance by selecting one representative galaxy for each of the five general morphological categories (defined previously in this sec-

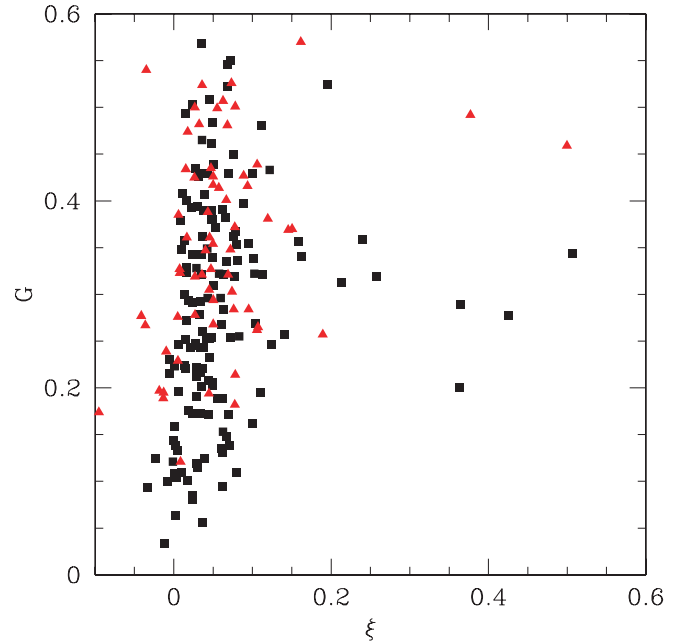


FIG. 7.—Distribution of  $G$  (Gini) vs.  $\xi$  (color dispersion) for galaxies in the  $z \sim 2$  (black squares) and  $z \sim 3$  (red triangles) samples. Note that a few extreme outliers from this trend lie outside the visible region of this plot to better illustrate the main correlation.

tion), artificially redshifting them through the range  $z = 1.8$ – $3.4$ , and measuring the resulting morphologies using our variable threshold pixel selection technique. As illustrated by Figure 8, in most cases we would measure consistent values for the morphological parameters for a given galaxy if it were located at any redshift throughout our sample. This constancy fails, however, for the most faint and nebulous of objects ( $G \lesssim 0.15$ , green dot-dashed line in Fig. 8), for which the multiplicity  $\Psi$  and the color dispersion  $\xi$  can vary substantially because the number of pixels in the segmentation map is small and random variations in noise can drastically affect both the locations of selected pixels (to which  $\Psi$  is particularly sensitive) and the residual color (to which  $\xi$  is sensitive). Such objects represent less than 20% of the sample, however, and the importance of this effect on  $\Psi$  may be mitigated by noting that  $\Psi$  is only well defined up to  $\Psi \sim 25$ . We also note a slight decrease in  $I$  with redshift to  $z = 3$ , followed by a smaller upturn at  $z > 3.3$ . The first of these effects is consistent with our neglect of the change in angular size with redshift, and the second with the inclusion of a small number of sky pixels in the segmentation map when the selection threshold is pushed down to  $3\sigma$ . Neither effect is large enough to noticeably impact our analysis.

Having demonstrated the uniformity of the selection technique, we consider what (if any) information is lost for galaxies in the lower end of the redshift range by effectively restricting our analysis to those pixels brighter than about  $10\sigma$  above the background sky noise. In Figure 9 we plot morphological parameters calculated for the same five galaxies as before for a range of surface brightness selection thresholds. Most obviously,  $I$  decreases rapidly with increasing brightness threshold since correspondingly fewer pixels are included in the segmentation map. In addition,  $G$  declines noticeably as the lower flux population is gradually omitted from the map. In contrast,  $\Psi$  and  $\xi$  remain relatively constant throughout the range of selection thresholds considered, with the exception of purely nebulous sources (dot-dashed green line) for which we have previously noted the instability of these

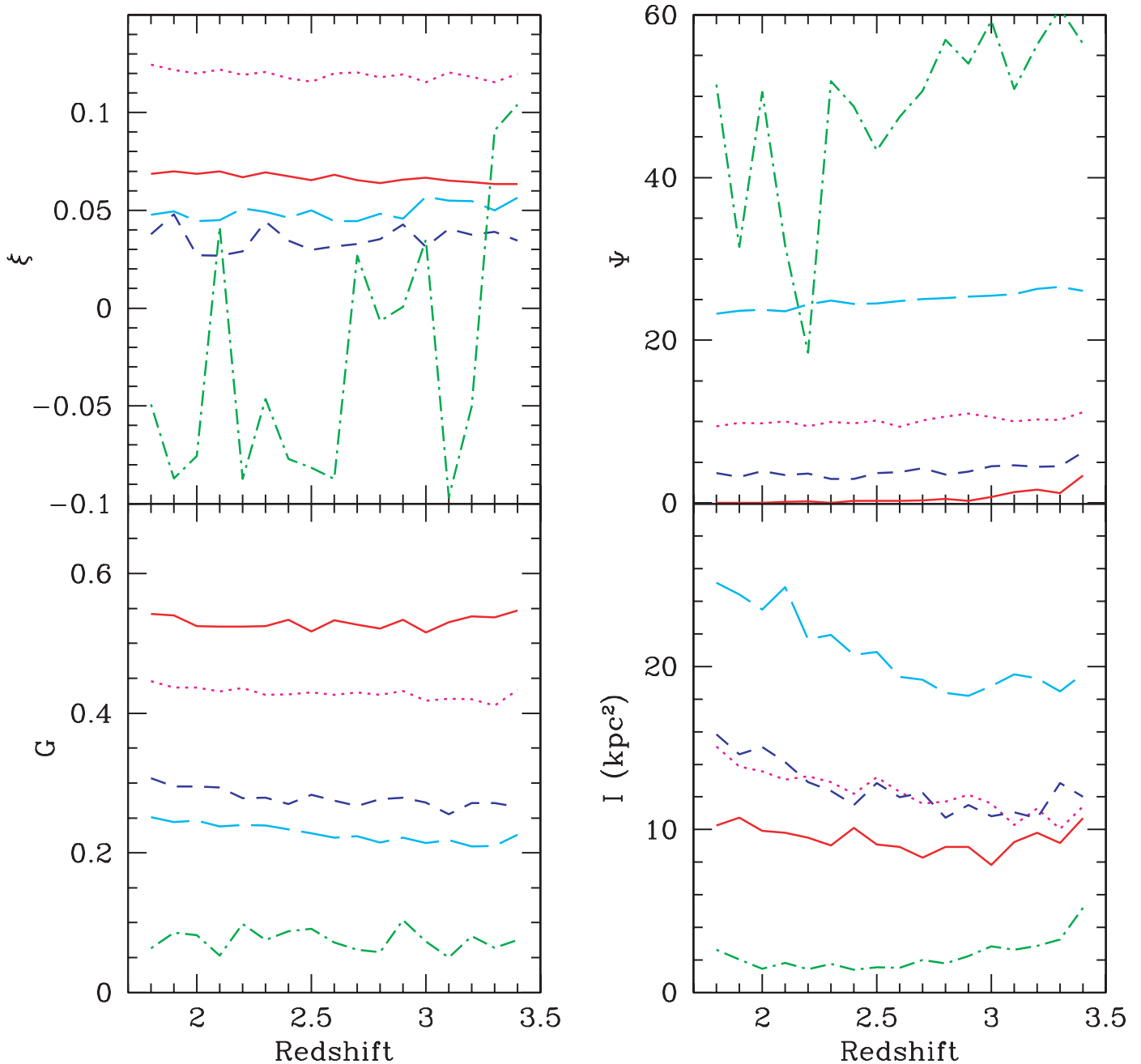


FIG. 8.—Robustness of morphological parameters to redshift when using the variable surface brightness method to define the segmentation map. Colored lines indicate the trends found by artificially redshifting one representative galaxy from each of the five general morphological classes through the range  $z = 1.8$ – $3.4$  before performing morphological analysis. These five classes (defined in § 3) and their representative galaxies are as follows: single nucleated source (BX 1040; *solid red line*), multiple nucleated source (BX 1630; *dotted magenta line*), single nucleated source with nebulosity (BX 1297; *short-dashed dark blue line*), multiple nucleated source with nebulosity (BX 1035; *long-dashed cyan line*), and purely nebulous source (BX 1169; *dot-dashed green line*).

two parameters. Most importantly, however, if we neglect purely nebulous sources, we note that the same *relative* information is preserved at all brightness thresholds: no matter what the threshold it is equally possible to distinguish between the galaxy types despite the overall trends. That is, since the lines do not cross (again with the exception of the green dot-dashed line and  $\xi$  at very low thresholds), we may be confident that we are not discarding information by using a  $\sim 10 \sigma$  segmentation map at lower redshifts.

We now note a few caveats to this analysis that should be borne in mind. First, by using a fixed bandpass, we have measured the morphologies of  $z \sim 2$  and  $z \sim 3$  galaxies at slightly different rest

wavelengths. However, this effect should be negligible since our morphological parameters do not change substantially using data from the  $B$ ,  $V$ , or  $I$  bandpasses (although they can change somewhat in the  $z$  bandpass due to the lower signal-to-noise ratio for all detections at NIR wavelengths). Parameters calculated in each of these bands correlate very strongly with one another, differences being dominated by the limiting surface brightness reached in each band. Given that our sample consists of actively star-forming galaxies, this is perhaps not surprising since young massive stars tend to dominate the spectral energy distribution (SED) out to at least rest-frame blue wavelengths. Second, we have neglected surface brightness evolution throughout our sample. Since our primary

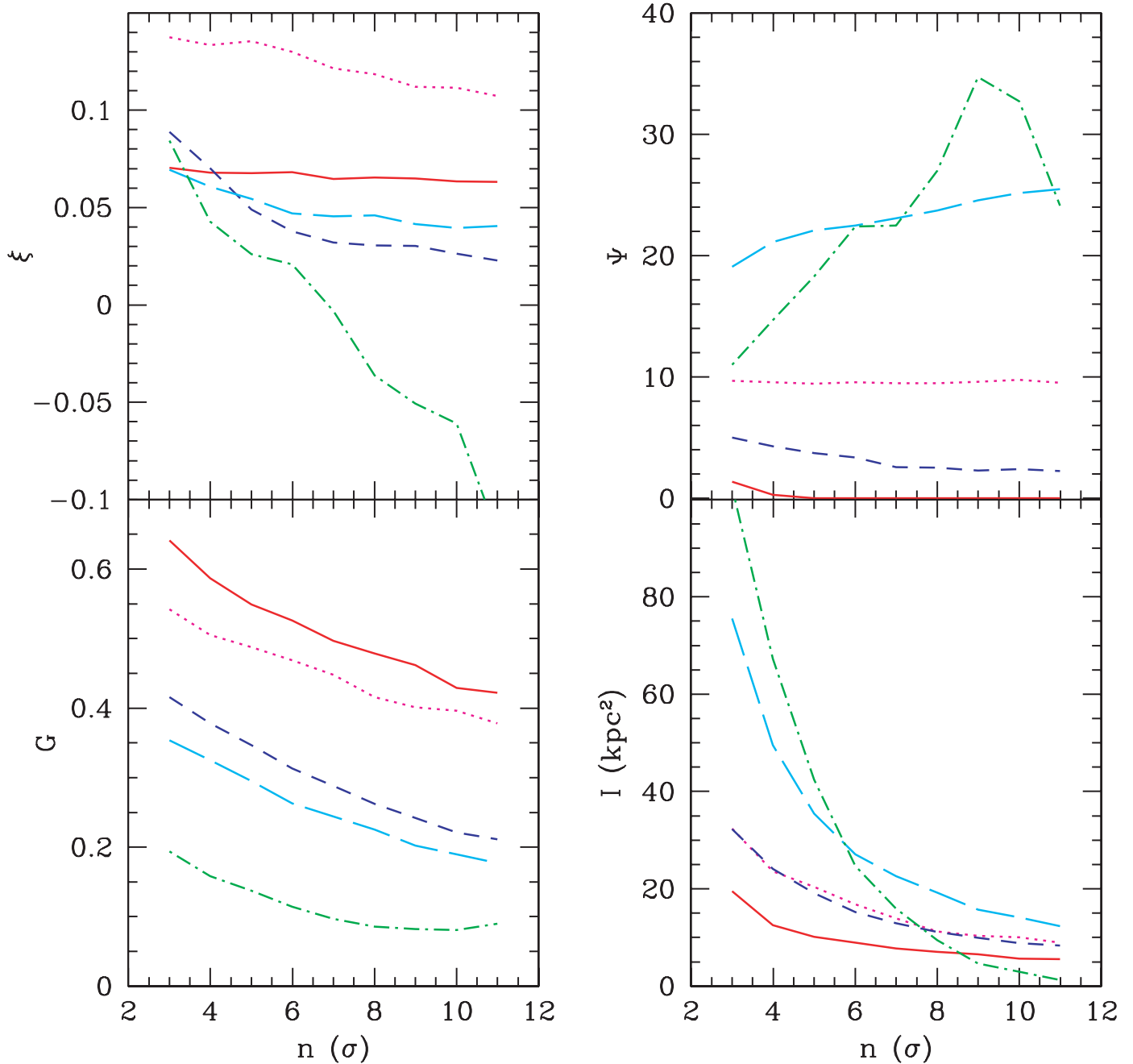


FIG. 9.—Same as Fig. 8, but plotting the calculated values of morphological parameters for the five classes of galaxies as a function of the adopted surface brightness selection threshold in multiples of the background sky noise  $\sigma$ . Note for comparison that segmentation maps corresponding to the 3, 5, and 10  $\sigma$  selection regions for BX 1035 (*long-dashed cyan line*) are shown in Fig. 3.

goal is to investigate the physical meaning of morphology rather than providing a detailed comparison between samples at different redshifts, we choose not to introduce uncertain corrections for such effects into our analysis. Third, it is possible that some regions of flux included in our segmentation maps are due to chance alignments of some object at a very different redshift than the target galaxy. However, we judge this to be an unlikely major source of contamination to our sample since (1) the various pieces of the galaxies have consistent colors and (2) the total number density of optically selected  $z \sim 2-3$  galaxies is  $\sim 10 \text{ arcmin}^{-2}$  to  $\mathcal{R} = 25.5$  (Steidel et al. 2004), giving a low probability for chance supposition of two unrelated galaxies within  $1.5''$ . Finally, we have made no correction for the effects of galaxy inclination to the line of sight. While it is conceivable, and indeed likely, that some

of the variance in apparent morphology may be due simply to different orientations relative to the line of sight, our knowledge of these galaxies is at present insufficient to allow us to compensate for such effects in any meaningful way.

Of the four parameters that we have introduced, the  $G$ - $\Psi$  classification scheme best reproduces the morphological trends apparent to the eye. This system is illustrated in Figure 10, which shows a representative set of galaxies from our sample and demonstrates how these two parameters serve to distinguish galaxies based on their degree of nucleation and number of components. Since surface brightness dimming and bandshifting make it difficult to associate the morphologies of  $z \sim 2-3$  sources with galaxies in the local universe, we avoid such direct, and potentially misleading, comparisons. We describe the *sense* of our

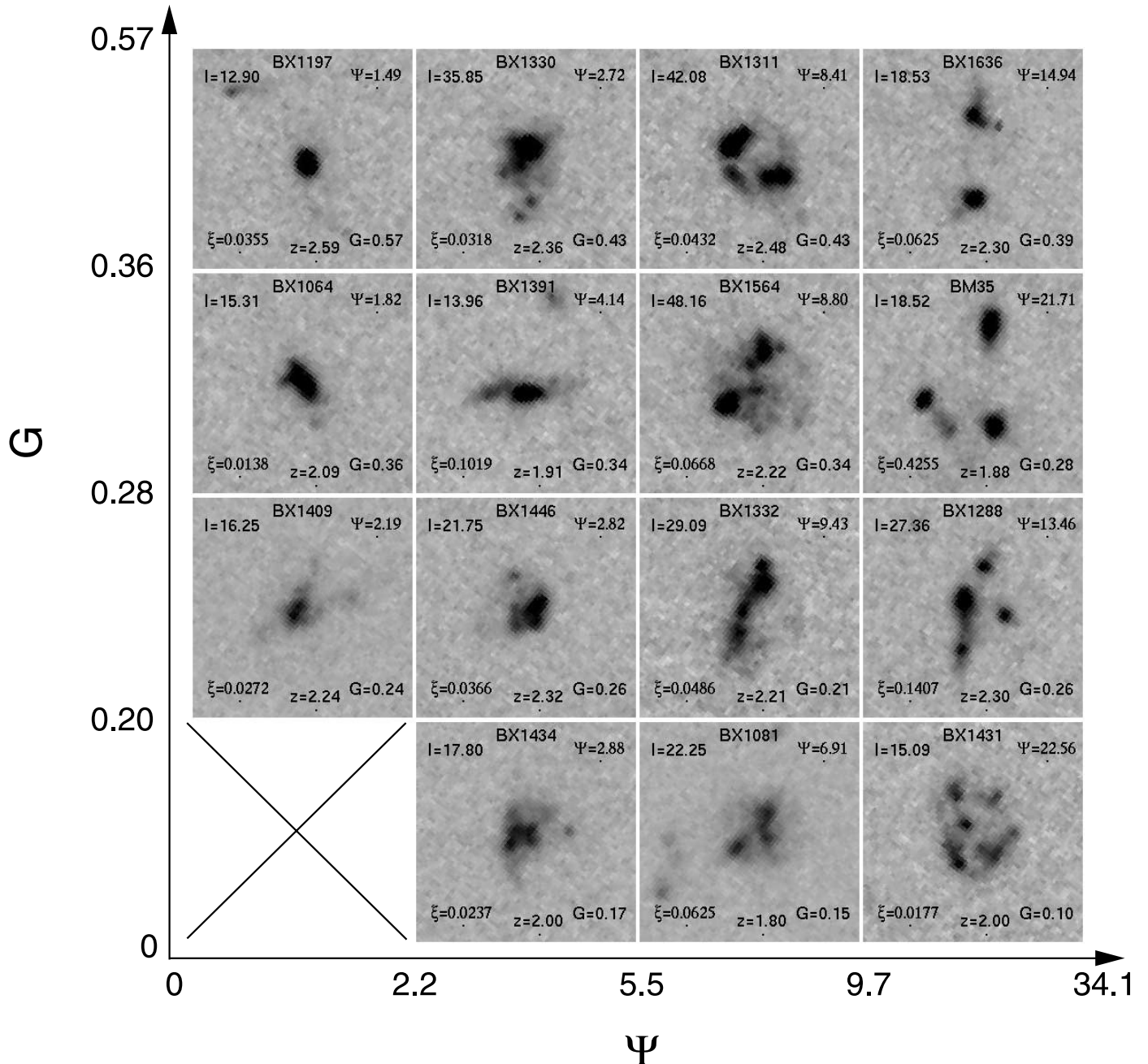


FIG. 10.—Same as Fig. 2, but for the *HST* ACS rest-UV morphologies of redshift  $z \sim 2$  galaxies classified according to Gini ( $G$ ) and multiplicity ( $\Psi$ ) parameters. Horizontal and vertical bin ranges are chosen to divide the sample into quartiles. Increasing values of  $G$  correspond to increasing nucleation of source emission, and increasing values of  $\Psi$  correspond to increasing number of components.

classification parameters by noting, however, that early-type galaxies typically are larger (i.e., larger  $I$ ), more concentrated (larger  $G$ ), less multiple (lower  $\Psi$ ), and have lower color dispersion ( $\xi$ ) than their late-type counterparts, which are instead dominated by emission from multiple scattered knots of star formation. A more thorough overview of the relation between local and high-redshift galaxies is given by LPM04.

#### 4. OVERVIEW OF REST-UV SPECTRA

##### 4.1. Spectral Processing

As part of an ongoing Keck LRIS-B spectroscopic survey (Steidel et al. 2004) we have compiled UV spectra of our 216 target galaxies in the GOODS-N field and here explore how these

spectra correspond to the morphology of their host galaxies. Unfortunately, spectra of individual galaxies are rarely of sufficient quality to accurately measure the strengths of their emission/absorption components, and we therefore divide the spectra into five bins according to each of our four morphological parameters and measure the strengths of features in stacks of the spectra within these bins. We find that five bins gives a suitably large number of bins across which spectroscopic trends may be assessed while still producing reasonable quality stacked spectra (each comprised of 30 galaxies at  $z \sim 2$  and 13 galaxies at  $z \sim 3$ ).

Our spectroscopic combination method is similar to that described by Shapley et al. (2003). Before stacking, individual sky-subtracted spectra were flux-calibrated and shifted to the systemic rest frame using the prescriptions given by Adelberger et al. (2005),

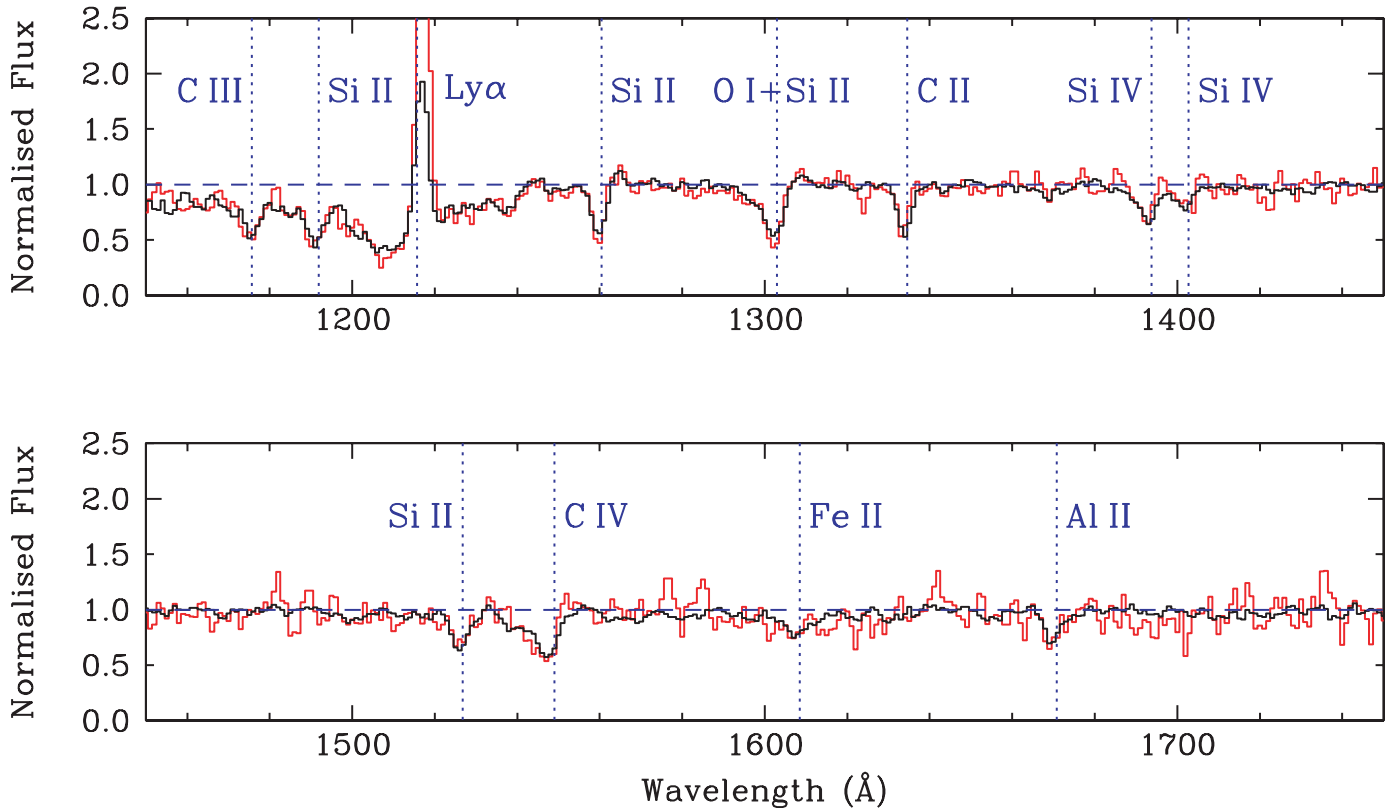


FIG. 11.—Stacked continuum-normalized spectra are plotted for all 150  $z \sim 2$  and 66  $z \sim 3$  galaxies (black and red lines, respectively). Labels and dotted lines indicate the fiducial locations of atomic transitions corresponding to major spectroscopic features. Note that Ly $\alpha$  emission is considerably stronger in the  $z \sim 3$  sample and peaks at a relative normalized flux of 3.95 (not shown for clarity).

then resampled to a common dispersion of  $1 \text{ \AA pixel}^{-1}$  and re-scaled to a common mode in the range 1250–1500  $\text{\AA}$ . Spectra were manually cropped to eliminate overly noisy segments due to falloff of the LRIS-B blue-side efficiency and of the red-side dichroic transmission. The resulting spectra were averaged using a min/max rejection of hot pixels, cosmic rays, and bad sky subtraction events; three high and low values were rejected at each dispersion coordinate (corresponding to a rejection of the high/low 10% for the  $z \sim 2$  sample). Continuum normalization was performed by iteratively fitting a spline function to the stacked spectrum using wavelength intervals selected to be free of strong interstellar features, giving results consistent with the normalization method described by Rix et al. (2004).

#### 4.2. Key Spectral Features

The rest-frame ultraviolet (1000–1800  $\text{\AA}$ ) spectra of rest-UV color-selected galaxies are typified (Fig. 11) by redshifted Ly $\alpha$  emission superposed on a broad blueshifted resonant absorption trough and by strong velocity-broadened absorption lines due to energetic galaxy-scale outflows (Shapley et al. 2003). The strength of Ly $\alpha$  emission is originally governed by the rate of star formation and initial mass function (IMF) in galactic H II regions, although this raw flux is significantly modified by resonant scattering from interstellar H I, generally culminating in its eventual absorption by interstellar dust and subsequent reradiation in the infrared. The observed Ly $\alpha$  emission strength is therefore a complex function of neutral hydrogen column density, dust fraction, and geometric/kinematic projection of the outflowing interstellar medium (ISM) on the line of sight. Typically, observed Ly $\alpha$  emission is redshifted by roughly  $400 \text{ km s}^{-1}$  relative to the systemic velocity (Shapley et al. 2003; Steidel et al. 2004), corre-

sponding to scattering from the back side of outflowing ISM, from which the Doppler shift is suitable to take the photon off of resonance and permit it to escape the galaxy.

Other notable features include strong, optically thick absorption lines from low-ionization species (e.g., Si II  $\lambda 1192$ , Si II  $\lambda 1260$ , O I+Si II  $\lambda 1303$ , C II  $\lambda 1334$ , Si II  $\lambda 1526$ , Fe II  $\lambda 1608$ , and Al II  $\lambda 1671$ ) arising from outflowing neutral ISM. As shown in Figure 11, these absorption lines are blueshifted from the systemic redshift, corresponding to absorption from outflowing gas seen from the nearby side of a galaxy-wide outflow: their full widths can reach  $\sim 1000 \text{ km s}^{-1}$  (Pettini et al. 2002; Shapley et al. 2003). We note that while O I+Si II  $\lambda 1303$  (a blend of the low-ionization species O I  $\lambda 1302$  and Si II  $\lambda 1304$ ) appears to be blended with a third component around 1297  $\text{\AA}$  (resulting in a shallower blue-side slope for the composite line), it is generally possible to deblend this additional component to measure O I+Si II  $\lambda 1303$  alone. This broad  $\lambda 1297$  feature is likely itself a blend of the stellar photospheric lines C III  $\lambda 1296.33$ , Si III  $\lambda 1294.54$ , Si III  $\lambda 1296.73$ , and Si III  $\lambda 1298.93$  (C. A. Tremonti et al. 2007, in preparation), variations in the relative strengths of which can shift the apparent centroid of the  $\lambda 1297$  blend from  $\lambda = 1295$  to 1298  $\text{\AA}$ .

Also apparent are absorption lines due to higher ionization species, including the Si IV  $\lambda\lambda 1393, 1402$  doublet and C IV absorption around 1549  $\text{\AA}$ . Although all of these lines are blended with stellar features, C IV is a particularly complex blend of interstellar absorption lines at 1548 and 1550  $\text{\AA}$ , combined with a P Cygni component from the winds of the most luminous O and B stars. We neglect the numerous additional features due to nebular, fine-structure, and stellar atmosphere transitions (e.g., C III  $\lambda 1176$ ; for a further list see Shapley et al. 2003), since they are not generally detected to high statistical significance after the sample has been

divided among five morphological bins. We refer the reader to Shapley et al. (2003) and references therein for further discussion of the physical interpretation of the rest-UV spectra.

#### 4.3. Equivalent Widths and Uncertainties

The equivalent widths of all absorption features were integrated nonparametrically relative to the normalized continuum. Generally, features shortward of Ly $\alpha$  and longward of 1500 Å are considerably noisier than those between these wavelengths, and we therefore define average “low-ionization” and “high-ionization” absorption line strengths ( $W_{\text{LIS}}$  and  $W_{\text{HIS}}$ , respectively) as the weighted means of the shorter wavelength transitions Si II  $\lambda$ 1260, O I+Si II  $\lambda$ 1303, and C II  $\lambda$ 1334 (for  $W_{\text{LIS}}$ ) and Si IV  $\lambda$ 1393 and 1402 (for  $W_{\text{HIS}}$ ).

The total equivalent width of the Ly $\alpha$  feature (i.e., absorption plus emission) tends to be strongly affected by the noisiness of the absorption trough, so we characterize the strength of the emission component alone. The equivalent width of emission ( $W_{\text{Ly}\alpha}$ ) is determined by dividing the total flux in the emission component by the continuum level that would be present in the absence of any absorption trough.

It is possible to assess the statistical significance of possible deviations from a constant value by using the  $\chi^2$  statistic

$$\chi^2 = \sum_i \left( \frac{x_i - \bar{x}}{\sigma_{\text{sample}}} \right)^2, \quad (8)$$

where  $x_i$  is the measured equivalent width for a given bin,  $\bar{x}$  is the mean equivalent width among all five bins, and  $\sigma_{\text{sample}}$  is the square root of the natural variance among samples of randomly binned spectra.<sup>13</sup> We find that  $\sigma_{\text{sample}}$  is considerably larger than the uncertainty in the mean equivalent width for a given stack (which belies the actual variance observed between randomly drawn samples) and therefore adopt it as a conservative means of ensuring that any possible trends are more significant than would be likely to occur randomly. As such, the significance of a particular value of  $\chi^2$  is evaluated using  $5 - 1 = 4$  degrees of freedom to give the likelihood  $P$  that deviations of the five measurements from a constant average value (whether in the form of a monotonic trend or a single bin whose equivalent width varies greatly from the average with respect to the expected variance) are greater than that expected from a random binning of the sample. Applying this method to our measurements from randomly selected quintiles of galaxies, we determine that a threshold of  $P > 90\%$  suffices to cull apparent associations due to random variance.

## 5. THE RELATION OF REST-UV MORPHOLOGIES TO SPECTRA

As described in § 4.1, we bin the galaxy sample separately into quintiles according to each of the morphological parameters  $I$ ,  $G$ ,  $\Psi$ , and  $\xi$ . Bin divisions are determined so that each bin contains an identical number of galaxies (i.e., 30 each for the  $z \sim 2$  sample, and 13 each for the  $z \sim 3$  sample); precise ranges are given in Table 1. In all cases our spectra are broadly consistent with the diffuse light spectrum of local starburst galaxies (e.g., Chandar et al. 2005), indicating that largely similar processes likely dominate the UV light output of all morphological types in our sample. Despite this general similarity, the spectra show some variation with morphology as demonstrated in Figure 12, which we proceed to discuss in detail.

We first note, however, the caveat that the position angles of the slits used to obtain our UV spectra have not been chosen to

TABLE 1  
QUINTILE BINS FOR MORPHOLOGICAL PARAMETERS

Parameter	$x_1^a$	$x_2$	$x_3$	$x_4$	$x_5$	$x_6$
$I (z \sim 2)$ .....	0.181	7.473	12.540	15.977	20.108	48.163
$I (z \sim 3)$ .....	4.200	11.559	13.952	17.991	21.407	45.181
$G (z \sim 2)$ .....	0.034	0.172	0.245	0.321	0.382	0.568
$G (z \sim 3)$ .....	0.105	0.265	0.321	0.385	0.459	0.570
$\Psi (z \sim 2)$ .....	-0.199	1.667	3.871	6.151	10.677	34.062
$\Psi (z \sim 3)$ .....	0.249	2.426	5.236	8.849	12.599	22.795
$\xi (z \sim 2)$ .....	-0.115	0.015	0.033	0.049	0.076	0.507
$\xi (z \sim 3)$ .....	-0.095	0.008	0.040	0.057	0.078	0.500

<sup>a</sup> Successive values of  $x_i$  denote boundary divisions between galaxies binned into equal-size quintiles according to each of the morphological parameters (without regard to the other three parameters).

correspond to the major axis of each of the galaxies, and it is therefore possible for a few of the most widely separated sources with multiple components that the UV spectra may represent only one of the components. Given the seeing-limited nature of the spectroscopic observations and the fact that the typical size of our targets ( $\sim 1''$ ) is less than the width of the LRIS-B slit ( $1.2''$ ), we doubt that this has a considerable effect. More likely perhaps is the probability that spectra are dominated by light from the bright nucleated regions of our sources and may not be expected to show any difference between nucleated and nucleated+nebulous sources if the spectra of the nucleated regions are similar in each case.

### 5.1. Interstellar Absorption Lines

As illustrated in Figure 12 (*middle rows*), we find that the strength of interstellar absorption lines ( $W_{\text{LIS}}$  and  $W_{\text{HIS}}$ ) is largely uncorrelated with UV morphology, although there appears to be a statistically significant ( $P = 92\%$ ) association of the strength of low-ionization species with galaxy size  $I$ . Indeed, the data may be consistent with a trend that larger galaxies tend to have stronger interstellar absorption lines. Such a trend is most apparent for the  $z \sim 2$  sample; while the  $z \sim 3$  sample suggests a similar trend, the greater statistical uncertainties mitigate its significance.

We explore this possible trend in greater detail for the  $z \sim 2$  sample by stacking our spectra in two dimensions to explore the variation of line strengths across a plane of two parameters smoothed by a variable-width kernel. We stack the spectrum of each galaxy with that of its 10 nearest neighbors in the  $I$ - $G$  plane to distinguish large nebulous objects from large yet nucleated objects, with interpoint “distances” along each axis normalized by the dynamic range of values along the axis. In Figure 13 we plot  $I$  versus  $G$  for  $z \sim 2$  galaxies, with point size corresponding to the strength of  $W_{\text{LIS}}$ . On the whole, the distribution of galaxies with strong and weak low ionization lines (i.e., large and small points) is quite similar, except for the lower left corner representing the faintest and most nebulous galaxies, for which there is an overabundance of small points (i.e., sources with weak  $W_{\text{LIS}}$ ). Given the similar overall distribution of line strengths, we conclude that the association between  $I$  and low-ionization absorption strength is due to the overrepresentation of weaker line sources among the faint and nebulous galaxy sample rather than to an overall trend. Although this may indicate a genuine physical characteristic, we note that it is this class of low surface brightness galaxies for which spectra are typically of the poorest quality and absorption-line measurements least reliable. It is interesting, however, to note that the high-ionization absorption lines do not likewise appear weaker in this class of galaxies (see Fig. 12) as might be expected

<sup>13</sup> Thirty samples were sufficient to converge  $\sigma_{\text{sample}}$  to within 5%.

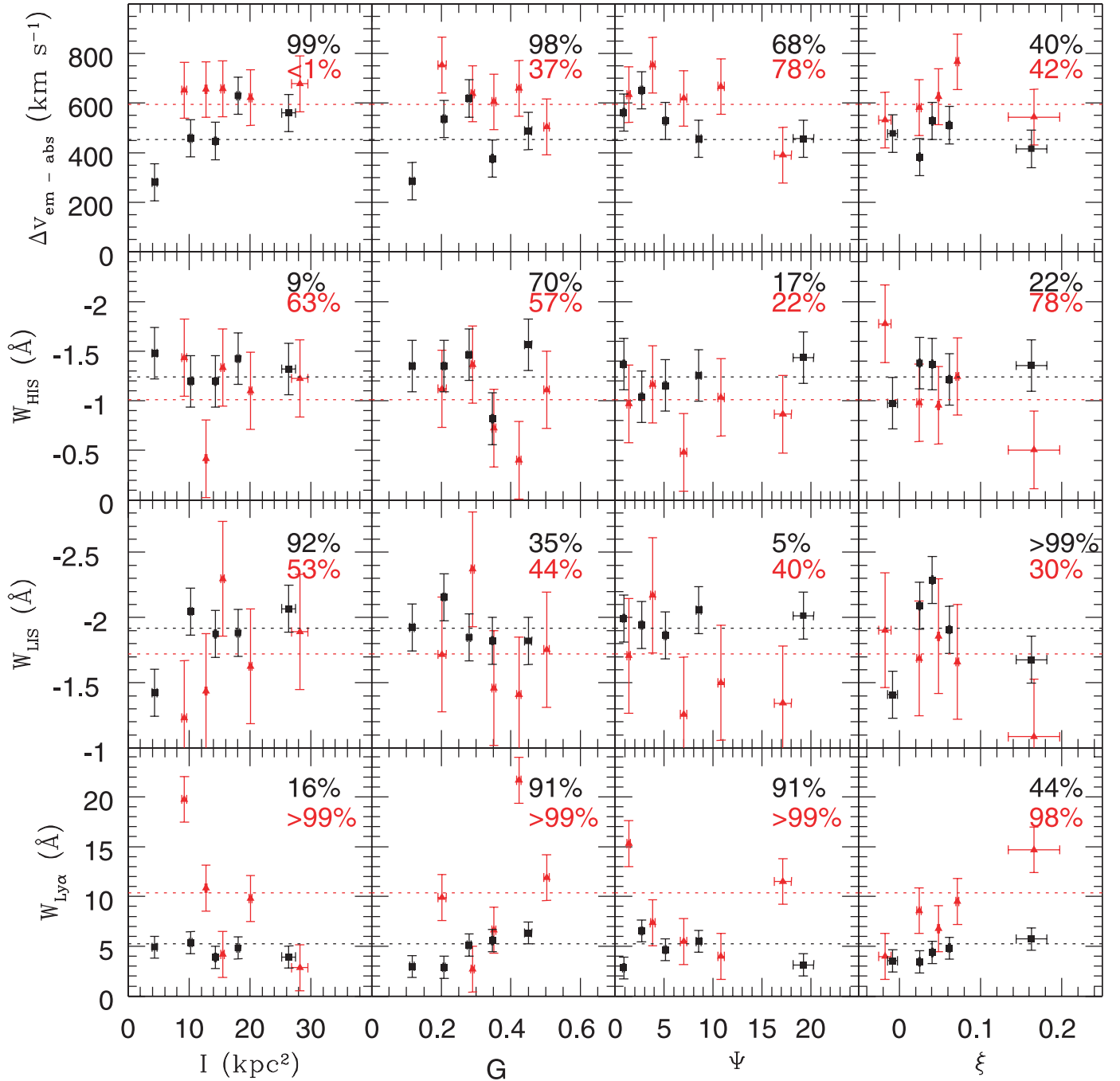


FIG. 12.—Ly $\alpha$  emission ( $W_{\text{Ly}\alpha}$ ) equivalent width, low- and high-ionization interstellar absorption equivalent width ( $W_{\text{LIS}}$  and  $W_{\text{HIS}}$ , respectively), and the kinematic offsets between emission and absorption lines ( $\Delta v_{\text{em-abs}}$ ) measured from quintiles in the morphological parameters  $I$  (size),  $G$  (nucleation),  $\Psi$  (multiplicity), and  $\xi$  (color dispersion). Black and red symbols represent data from the  $z \sim 2$  and  $z \sim 3$  samples, respectively, shown with error bars representing the standard deviation among measurements made from randomly binned samples. Red and black dotted lines indicate the values measured for the complete  $z \sim 2$  and  $z \sim 3$  stacks, respectively, while the black and red percentages given in each panel indicate the  $\chi^2$  probability  $P$  that the data points shown are statistically inconsistent with a constant value. Generally, values of  $P > 90\%$  are indicative of significant deviation: note particularly the linear trends of Ly $\alpha$  emission increasing for more nucleated sources (i.e., those with higher  $G$ ) and low-ionization absorption strength increasing for larger sources (i.e., those with greater  $I$ ).

were the apparent decline in low-ionization line strength due to spectrum quality alone.

Figure 13 also introduces another curiosity, namely, the overabundance of weak-line objects in a line running through the plot from  $G, I = 0.2, 30 \text{ kpc}^2$  to  $G, I = 0.6, 10 \text{ kpc}^2$ . This band does not correspond to an obviously distinct class of galaxies or have any obvious reason for occupying the region of this plot that it does. We suggest the possibility that there could be a population of galaxies that have relatively weak outflowing components that

are somehow distinguishable in this plot, but we caution that random variation combined with the kernel smoothing technique might also be responsible for this enigmatic feature.

There is one additional significant deviation from uniformity for the color dispersion  $\xi$  and the low-ionization absorption line strength (at a significance level of  $>99\%$  for the  $z \sim 2$  sample). However, inspection of Figure 12 offers no clear explanation of the nature of this association: objects in both the smallest and largest bins of  $\xi$  have weaker absorption lines than objects in the

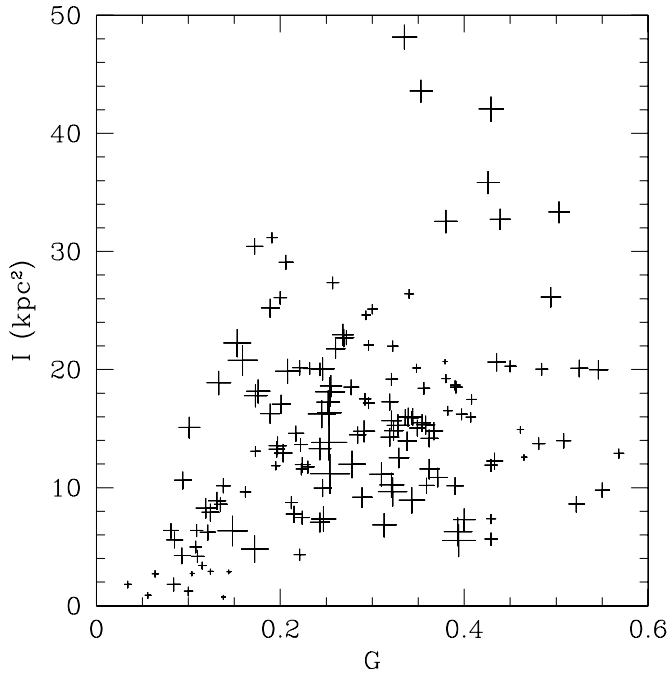


FIG. 13.—Low-ionization absorption line strengths for  $z \sim 2$  galaxies plotted (*plus signs*) according to their location in the size-Gini ( $I$ - $G$ ) plane; spectra of each galaxy have been stacked with those of their 10 nearest neighbors in this plane. Point sizes correspond linearly to the value of  $W_{\text{LIS}}$ . Note the overabundance of weak-absorption sources (*smaller symbols*) in the lower left corner of the plot and in the strip running from  $G, I = 0.2, 30 \text{ kpc}^2$  to  $0.6, 10 \text{ kpc}^2$ .

intermediate three bins, and there hence appears to be no particular *linear* correlation between the variables. While this deviation may be a genuine product of physical phenomena, its interpretation is unclear, particularly given the uncertain meaning of  $\xi$ .

### 5.2. $\text{Ly}\alpha$ Emission

As indicated by Figure 12 (*bottom row*), there are relatively many possible associations between  $\text{Ly}\alpha$  emission strength and galaxy morphology, the simplest of which to interpret is the positive correlation between  $\text{Ly}\alpha$  and the Gini coefficient  $G$ . These two parameters show a clear linear trend of increasing emission strength with increasing nucleation; for the  $z \sim 2$  sample the most strongly nucleated sources show roughly twice the emission seen in the most nebulous (see also Fig. 14), and for the  $z \sim 3$  sample an even stronger trend is possible (although less well defined). It is unlikely that this trend is due to substantial variation of the composition or velocity of interstellar gas since such variations should also affect the strengths of absorption lines, which remain statistically constant across all values of  $G$  (see Figs. 12 and 14). A more plausible explanation may be that dust might be present in greater quantities in nebulous low- $G$  sources, causing greater attenuation of  $\text{Ly}\alpha$  photons. Under this hypothesis, it may be simply the presence of more or less dust that determines both the observed degree of UV nucleation and the strength of resonant  $\text{Ly}\alpha$  emission. We explore this hypothesis further in § 6.

We map the  $\text{Ly}\alpha$  trend in greater detail in Figure 15, which compares the strength of the association between  $\text{Ly}\alpha$  and  $G$  with the previously known association between  $\text{Ly}\alpha$  and stellar mass  $M_*$  (i.e., that galaxies with higher stellar masses have lower average  $\text{Ly}\alpha$  emission strength; Erb et al. 2006b).<sup>14</sup> Figure 15 suggests

<sup>14</sup> We caution that despite the fact that  $G$  is correlated with  $W_{\text{Ly}\alpha}$  and  $W_{\text{Ly}\alpha}$  with  $M_*$ ,  $G$  itself is *not* correlated with  $M_*$  (see § 6), indicating that correlations are not necessarily commutative.

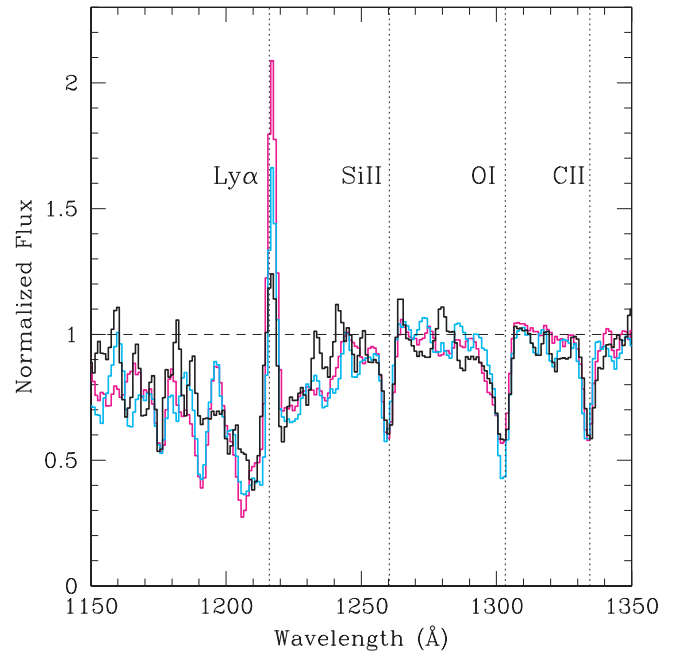


FIG. 14.—Stacked, continuum-normalized spectra for  $z \sim 2$  galaxies representing three bins in the morphological nucleation parameter  $G$ . The low- $G$  nebulous galaxy bin is represented by the black line, the intermediate bin by the cyan line, and the strongly nucleated sample by the magenta line. Spectra have been smoothed by a 3 pixel boxcar filter and normalized consistent with the prescriptions of Rix et al. (2004). Labels and dotted lines indicate the fiducial locations of major spectral features.

that the overall association between  $G$  and  $\text{Ly}\alpha$  is genuine, but that emission strength in fact peaks for galaxies with  $G \sim 0.4$  rather than for the few galaxies with  $G > 0.5$ . Since the galaxies with  $G > 0.5$  represent the extreme of nucleation and have much weaker  $\text{Ly}\alpha$  emission than expected based on the majority of the

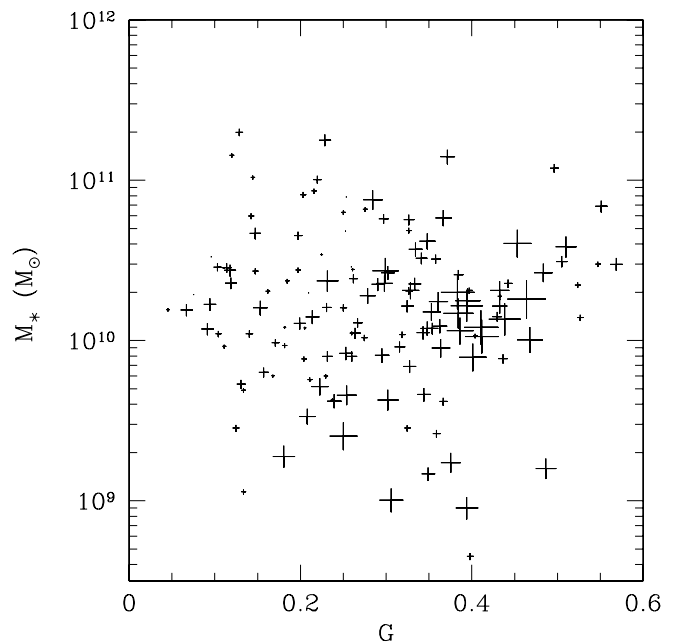


FIG. 15.— $\text{Ly}\alpha$  emission line strengths for  $z \sim 2$  galaxies plotted (*plus signs*) according to their location in the stellar mass-Gini ( $M_*$ - $G$ ) plane; spectra have been stacked with their 10 nearest neighbors in this plane as described in § 5.1. Point sizes correspond linearly to the value of  $W_{\text{Ly}\alpha}$ . Note the concentration of sources with strongest  $\text{Ly}\alpha$  emission around  $G \sim 0.4$  and  $M_* \sim 1.5 \times 10^{10} M_\odot$ .

galaxy sample, we posit that these few galaxies may be somehow distinct from the rest of the sample. Alternatively, the  $G \sim 0.4$  galaxies may represent a particularly dust-free population from which it is possible to see both star-forming regions and their surrounding material.

We also observe that  $W_{\text{Ly}\alpha}$  deviates from statistical uniformity when binned according to multiplicity  $\Psi$  (for both  $z \sim 2$  and  $z \sim 3$  samples), apparent size  $I$  (for the  $z \sim 3$  sample), and color dispersion  $\xi$  (for the  $z \sim 3$  sample). In the first case, there is less of an obvious trend in Figure 12 than an apparently random scatter of points, with particularly discrepant points found in both the highest and lowest bins in  $\Psi$ . In the latter two cases,  $W_{\text{Ly}\alpha}$  possibly declines with  $I$  and increases with  $\xi$  for the  $z \sim 3$  sample, but these trends are absent from the  $z \sim 2$  spectra. It is possible that these apparent deviations are due to the residual correlation between our morphological parameters (in which case the sense of a trend would be a complicated projection of the  $G$ - $W_{\text{Ly}\alpha}$  correlation onto the density distribution in morphology space), or simply that these deviations are telling us of some trend or population of galaxies that is not well distinguished using our chosen morphological parameters (or indeed any of the many others that we have explored). However, we are inclined (despite our conservative estimates of the uncertainty) to ascribe at least those deviations only visible in the  $z \sim 3$  spectra to statistical variance since similar trends do not appear in the much higher quality composite spectra from the  $z \sim 2$  galaxy sample.

### 5.3. Kinematic Offsets

Since our stacked spectra have all been shifted to the systemic rest frame (i.e., that of the stars and [H II] regions), it is possible to calculate the kinematic offset  $\Delta v_{\text{em-abs}}$  in each stack between Ly $\alpha$  emission and the average of the low-ionization absorption lines Si II  $\lambda$ 1260, O I+Si II  $\lambda$ 1303, and C II  $\lambda$ 1334. For the  $z \sim 2$  and  $z \sim 3$  samples, respectively, we find that  $\Delta v_{\text{em-abs}} = 453$  and  $594 \text{ km s}^{-1}$ , roughly similar to the Shapley et al. (2003) value of  $\Delta v_{\text{em-abs}} = 510 \text{ km s}^{-1}$  found for a large stack of 794  $z \sim 3$  LBG spectra.<sup>15</sup> While our relatively small sample of 66 spectra at  $z \sim 3$  is too noisy to distinguish any significant trends with morphology, for the  $z \sim 2$  sample  $\Delta v_{\text{em-abs}}$  is convincingly correlated with both the size parameter  $I$  and the Gini coefficient  $G$  (see Fig. 12, *top row*).

In particular, the offset velocity increases nearly linearly from  $\sim 300 \text{ km s}^{-1}$  for the smallest galaxies with  $I \sim 5 \text{ kpc}^2$  to near  $600 \text{ km s}^{-1}$  for the largest with  $I \sim 20 \text{ kpc}^2$ . The differences are similarly pronounced with respect to the Gini parameter  $G$ , but instead of increasing linearly through the sample, Figure 12 suggests that  $\Delta v_{\text{em-abs}}$  is lowest for galaxies with  $G \lesssim 0.2$ , peaks for intermediate values of  $G \sim 0.3$ , and possibly declines slightly at the most nucleated values of  $G \gtrsim 0.5$ . This high  $\Delta v_{\text{em-abs}}$  sample of high  $I$  and moderate to high  $G$  corresponds reasonably well to a particular morphological sample: the type 4 galaxies (as identified in § 3) that occupy a large angular area and tend to have bright nebulous emission paired with one or more distinct nucleations.

These data suggest that larger, more UV-luminous ( $I$  correlates well with UV luminosity; see § 6) galaxies on average may have stronger outflows than the rest of the population, as might be expected if these galaxies have particularly energetic input to their interstellar media and are therefore capable of blowing the most energetic outflows. We caution, however, that the major

discrepant point in both of these trends is for the most nebulous sample (i.e., that with both small  $I$  and small  $G$ ) whose UV spectra are fainter and typically of slightly lower quality.

Pairing this with the most significant understandable trend discovered in §§ 5.1 and 5.2, namely, the positive correlation between  $G$  and Ly $\alpha$  emission strength, we might be led to conclude that Ly $\alpha$  and  $\Delta v_{\text{em-abs}}$  are positively correlated, in contrast to the results of Shapley et al. (2003), who found that outflow velocities are slightly weaker for  $z \sim 3$  LBGs with strong Ly $\alpha$  emission. This discrepancy illustrates the important point that, given the large scatter in all of our correlations, *correlation is not commutative*. That is, while there is a general trend that Ly $\alpha$  emission strength increases for more nucleated objects, this nucleated population is not the same as that moderately nucleated, large- $I$  population for which  $\Delta v_{\text{em-abs}}$  peaks.

### 5.4. Rest-Optical Spectroscopic Features

As part of an ongoing NIR spectroscopic survey (Erb et al. 2006a), we have obtained rest-frame optical spectra in the wavelength regime of H $\alpha$  and [N II] for 19 of the 150 galaxies in the  $z \sim 2$  galaxy sample and use these spectra to explore whether there is any apparent relation between morphology and H $\alpha$  flux and/or the oxygen abundance as measured by the [N II]/H $\alpha$  ratio (Pettini & Pagel 2004). Given the extremely small sample of galaxies with NIR spectra, we divide these 19 galaxies into only three bins according to our morphological parameters and analyze the resulting stacked spectra (shown in Fig. 16) with a method similar to that adopted for the rest-UV spectra.

As indicated by the general similarity of all of the composites shown in Figure 16 and plotted more precisely in Figure 17, we find no significant variation in the strength of H $\alpha$  emission with rest-UV morphology. [N II] is only marginally detected in many of the composite spectra, and all variations are well within the uncertainty expected based on the noise of the composite spectra. We conclude therefore that to within the accuracy permitted by our small (and hence not fully representative of the large distribution of UV morphologies) spectroscopic sample the UV morphology of  $z \sim 2$  galaxies is uncorrelated with rest-frame optical spectroscopic features and the degree of metal enrichment as parameterized by the [N II]/H $\alpha$  oxygen abundance estimate.

## 6. THE ASSOCIATION OF REST-UV MORPHOLOGIES WITH PHOTOMETRICALLY DERIVED PROPERTIES

Using ground-based  $U_nGR$  and *Spitzer* MIPS photometry, it is possible to calculate the rest-frame,  $k$ -corrected luminosities of each of our target galaxies in the UV ( $L_{1600}$ ) and mid-IR ( $L_{5-8 \mu\text{m}}$ ),<sup>16</sup> in addition to estimating the total bolometric luminosity ( $L_{\text{bol}}$ ) and the ratio of IR/UV luminosities ( $L_{\text{FIR}}/L_{1600}$ ). The resulting SED from these and additional *JK* and *Spitzer* IRAC data may then be fitted with stellar population models to determine the best-fit stellar mass ( $M_*$ ), age, and optical extinction [ $E(B - V)$ ] for a given galaxy. Although the risk of confusion is greater in stellar population models based on such seeing-limited imaging, in almost all cases (except for those of the few most widely separated clumps) we find that the isophotes of the target galaxies reliably trace the ACS morphology, and all components are blurred together into a single object with minimal contamination from nearby sources. The comprehensive results of such efforts have been summarized by Reddy et al. (2006a); in the

<sup>15</sup> We note that the average velocity offset in *individual*  $z \sim 3$  LBG spectra with both emission and absorption components is typically  $\sim 650 \text{ km s}^{-1}$ ; see Shapley et al. (2003) for details.

<sup>16</sup>  $L_{1600}$  typically ranges from  $\sim 10^{10}$  to  $1.2 \times 10^{11} L_{\odot}$ ,  $L_{5-8 \mu\text{m}}$  from  $\sim 5 \times 10^9$  to  $1.3 \times 10^{11} L_{\odot}$ ; see Reddy et al. (2006a) for further details.

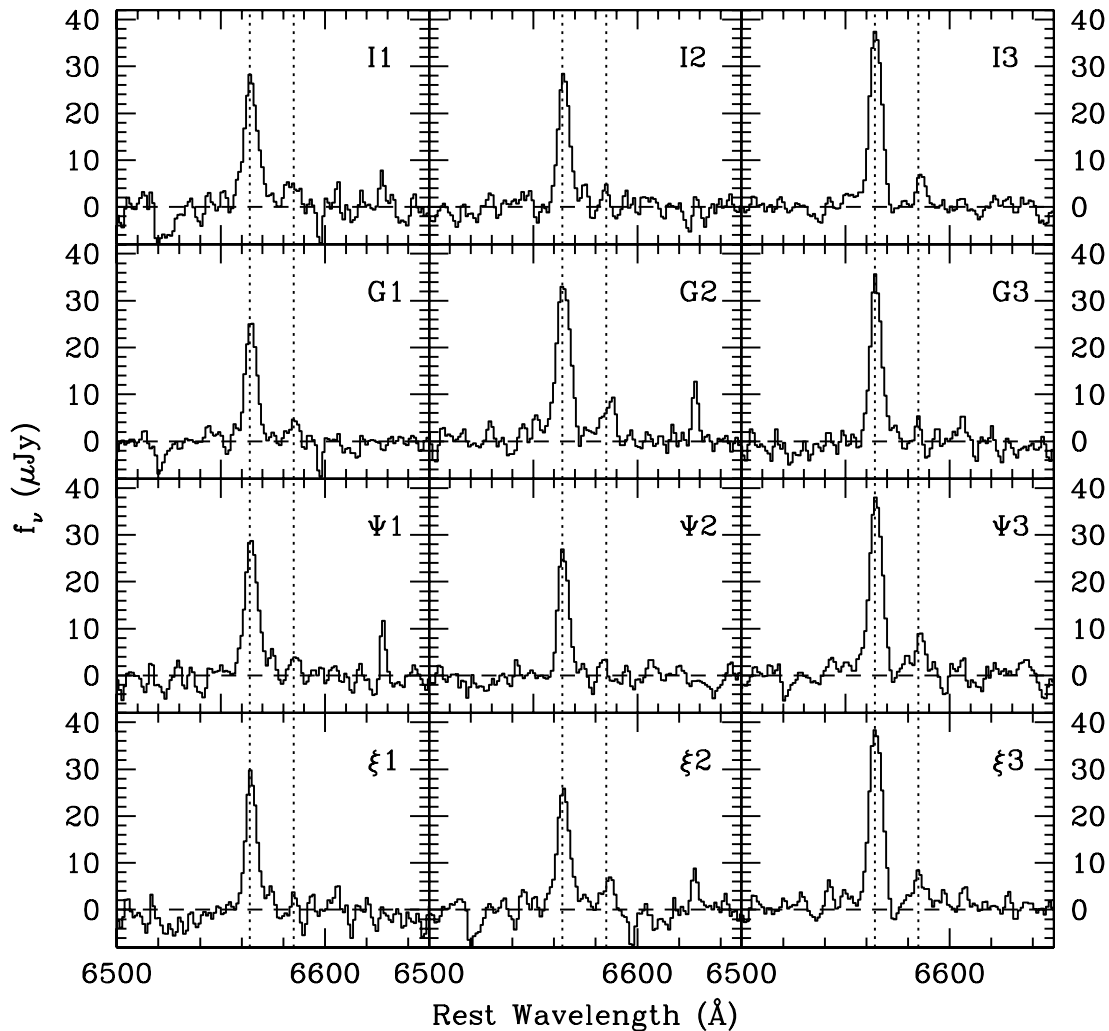


FIG. 16.—Flux-calibrated, composite H $\alpha$  spectra plotted for each of three bins in the morphological parameters  $I$  (size),  $G$  (Gini),  $\Psi$  (multiplicity), and  $\xi$  (color dispersion). Spectra are numbered according to increasing values of the morphological parameter (e.g.,  $G3$  is composed of more nucleated sources than  $G1$ ). The fiducial wavelengths of H $\alpha$  and [N II]  $\lambda 6583$  are indicated by dotted lines. Note that the strength of H $\alpha$  and [N II] is not significantly different in any of these panels.

present contribution we test the degree of association between morphology and such photometrically derived parameters. In this section we consider only the 62% of the  $z \sim 2$  sample of galaxies for which *Spitzer* MIPS 24  $\mu\text{m}$  detections directly measure the strength of rest-frame mid-IR emission (see further discussion in Reddy et al. 2006b).

We quantify the degree of association using the Spearman non-parametric rank correlation coefficient  $r_s$ , values of which are assessed in terms of their two-sided significance  $t$ . This significance gauges the probability that the null hypothesis (i.e., that there is no correlation between the two parameters) is true and that any apparent correlation is due to random chance alone. In Table 2 we calculate  $t_\sigma$ <sup>17</sup> for a grid of photometric versus morphological parameters (adopting the convention that positive  $t_\sigma$  indicates a positive correlation, and negative  $t_\sigma$  a negative correlation), denoting with an asterisk those for which the null hypothesis is less than 10% probable (i.e.,  $|t| < 0.1$ ,  $|t_\sigma| > 1.65$ ). We note from Table 2 that the null hypothesis is rejected in very few cases, indicating that in general morphology is largely decoupled from photometrically derived parameters.

<sup>17</sup> Since  $t$  is an awkward statistic to print for extremely small values, we instead give results in terms of  $t_\sigma$  corresponding to the number of sigma that  $t$  lies out along the wings of a Gaussian probability distribution.

The most significant correlations relate galaxy size ( $I$ ), nucleation ( $G$ ), and rest-frame ultraviolet luminosity ( $L_{1600}$ ) in the sense that larger and more strongly nucleated galaxies tend to have brighter UV continua. In general, these correlations are unsurprising since  $I$  effectively measures the number of UV-bright pixels in a galaxy (and a galaxy with large  $I$  is hence likely to have a large total UV luminosity), and high values of  $G$  are produced by relatively high concentrations of flux in a small percentage of the total number of UV-bright pixels (which occurs more commonly in galaxies with a high total UV luminosity to distribute). However, we note that the positive correlation between  $G$  and  $L_{1600}$  may also (at least in part) have a more physical explanation; if indeed nebulous low- $G$  sources are dustier, then UV radiation from these galaxies would be more strongly attenuated than from less dusty high- $G$  galaxies, contributing to the observed trend.

The next most significant correlations relate  $I$ ,  $G$ ,  $E(B - V)$  (the estimated reddening based on stellar population models and the far-UV spectral slope), and the ratio of IR to UV luminosity ( $L_{\text{FIR}}/L_{1600}$ , a proxy for UV attenuation). As quoted in Table 2,  $I$  and  $G$  are both negatively correlated with  $E(B - V)$  and  $L_{\text{FIR}}/L_{1600}$  (at levels of significance ranging from about 2 to 3  $\sigma$ ) in the sense that the most attenuated galaxies tend to have smaller UV-luminous areas (low  $I$ ) with weaker nucleation in the flux distribution (low  $G$ ). Although this correlation contains a great

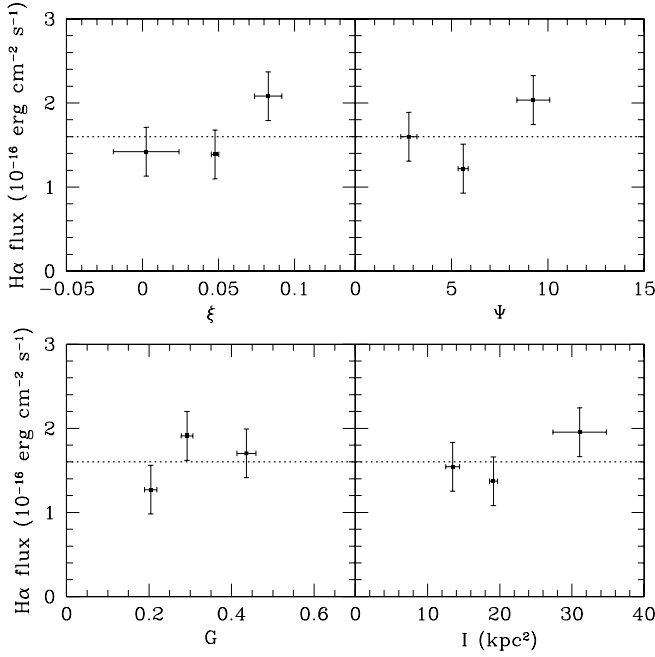


FIG. 17.— $H\alpha$  fluxes measured for the composite stacks in each of the morphological parameters  $I$  (size),  $G$  (Gini),  $\Psi$  (multiplicity), and  $\xi$  (color dispersion). Horizontal error bars represent uncertainty in the mean value of a morphological quantity within each bin; vertical error bars represent  $1\sigma$  uncertainties on the flux based on random draw tests. The dotted line in each panel represents the mean  $H\alpha$  flux of the entire sample.

deal of scatter and does not hold precisely for every galaxy (i.e., not all “small and nebulous” galaxies are highly extinguished), it nonetheless appears that *statistically* the most extinguished galaxies tend to be smaller and more nebulous than the general population. As previously hypothesized on the basis of  $Ly\alpha$  emission strength, it may therefore be the case that galaxy morphology is dictated in part by the presence and location of dust that partially extinguishes the UV continuum radiation and causes galaxies to appear slightly smaller (to a fixed limiting surface brightness) and more nebulous.

The color dispersion  $\xi$  appears to follow the trends found for  $I$  and  $G$  with UV luminosity and extinction (although at lower

TABLE 2

STANDARD DEVIATIONS FROM THE NULL HYPOTHESIS FOR INDEPENDENCE BETWEEN MORPHOLOGICAL AND PHOTOMETRIC PARAMETERS

Quantity	$I$	$G$	$\Psi$	$\xi$
$L_{1600}$ <sup>a</sup> .....	+6.39*	+4.57*	-0.32	+3.10*
$L_{5-8\mu m}$ <sup>b</sup> .....	+0.92	-0.10	+0.68	-0.30
$L_{5-8\mu m}$ <sup>c</sup> .....	+0.21	+0.59	+0.02	+0.68
$L_{FIR}/L_{1600}$ <sup>d</sup> .....	-3.33*	-1.85*	-0.22	-1.22
$L_{bol}$ <sup>e</sup> .....	+0.71	+0.90	+0.03	+0.73
$M_*$ <sup>f</sup> .....	+0.98	-0.05	-0.99	+0.07
$Age$ <sup>g</sup> .....	-0.83	-0.02	-0.16	+1.12
$E(B-V)$ <sup>h</sup> .....	-3.29*	-2.35*	-0.68	-1.84*

NOTES.—A plus sign denotes positive correlation, while a negative sign denotes negative correlation. Asterisks indicate correlations of greater than 90% confidence.

<sup>a</sup> Rest-frame ultraviolet luminosity.

<sup>b</sup> Rest-frame mid-IR luminosity (all sources).

<sup>c</sup> Rest-frame mid-IR luminosity (MIPS sources only).

<sup>d</sup> Ratio of far-IR to ultraviolet luminosities.

<sup>e</sup> Bolometric luminosity.

<sup>f</sup> Stellar mass.

<sup>g</sup> Age of stellar population.

<sup>h</sup> Estimated reddening based on far-UV spectral slope.

TABLE 3

STANDARD DEVIATIONS FROM THE NULL HYPOTHESIS FOR INDEPENDENCE OF MORPHOLOGICAL PARAMETERS AND STAR FORMATION

Quantity	$I$	$G$	$\Psi$	$\xi$
$SFR_{SED}$ <sup>a</sup> .....	-0.32	+0.59	-0.15	+0.30
$SFR_{UV}$ <sup>b</sup> .....	+8.04*	+4.77*	+0.46	+3.15*
$SFR_{IR}$ <sup>c</sup> .....	+0.21	+0.59	+0.02	+0.47
$SFR_{UV+IR}$ <sup>d</sup> .....	+0.92	+1.05	+0.03	+0.87
$SFR_{UV+IR}$ <sup>e</sup> .....	+5.67*	+2.17*	+0.80	+1.76*
$\phi^f$ .....	+1.24	+1.62	+0.88	+1.01
$\phi^g$ .....	-1.12	-0.43	-0.04	-0.70

NOTES.—A plus sign denotes positive correlation, while a negative sign denotes negative correlation. Asterisks indicate correlations of greater than 90% confidence.

<sup>a</sup> Star formation rate estimated from SED fitting.

<sup>b</sup> Star formation rate estimated from UV photometry.

<sup>c</sup> Star formation rate estimated from IR photometry.

<sup>d</sup> Star formation rate estimated from UV+IR photometry, MIPS-detected sources only.

<sup>e</sup> Star formation rate estimated from UV+IR photometry, MIPS-undetected sources only.

<sup>f</sup> Specific star formation rate,  $\phi = SFR_{UV+IR}/M_*$ . MIPS-detected sources only.

<sup>g</sup> Specific star formation rate,  $\phi = SFR_{UV+IR}/M_*$ . MIPS-undetected sources only.

significance), possibly due to its known positive correlation with  $G$ . The multiplicity parameter  $\Psi$ , however (also loosely correlated with  $G$ ), exhibits no statistically significant associations with any of the photometrically derived quantities presented in Table 2. In addition, we note that contrary to possible expectations (e.g., that galaxies with higher stellar mass might, analogously to local elliptical galaxies, appear morphologically more evolved and distinct from those with low stellar mass), there is no evidence for a relationship between stellar mass and UV morphology, implying that through a combination of physical processes galaxies ranging over two decades in stellar mass from  $M_* \sim 10^9$  to  $10^{11} M_\odot$  somehow appear visually indistinguishable. However, while no significant *overall* correlation was found by the Spearman test, almost all (20/22) of the most strongly nucleated sources ( $G > 0.4$ ) have masses greater than  $10^{10} M_\odot$  in contrast to those with  $G < 0.4$ , which span a full two decades in stellar mass.

In Table 3 we compare rest-UV morphologies to SFR estimates based on SED fitting and UV and IR continuum emission. Although these estimates tend to be loosely correlated with each other, there is considerable scatter in individual estimates of the SFR for a particular source using different methods. The least reliable of our estimates are the SFRs estimated from normalization of stellar population models (Shapley et al. 2005; Erb et al. 2006a; Reddy et al. 2006a), for which we find no significant correlations with morphological parameters (due either to the intrinsic lack of such a correlation or to the uncertainty inherent in the SFR estimate given by this method). The next most reliable estimate is that based on UV continuum flux, for which we calculate the uncorrected SFR based on  $U_nGR$  photometry and the conversion factor given by Kennicutt (1998). As shown in Table 3, the uncorrected UV SFR is strongly correlated with all morphological parameters save the multiplicity  $\Psi$ . However, this is not surprising given the strong association between total UV luminosity and morphology shown in Table 2. While it is likely that large (high  $I$ ), nucleated (high  $G$ ) objects have a higher than average rate of *uncorrected* star formation, it is not necessarily true that the same holds for the total SFR. Indeed, in the majority of cases *obscured* star formation comprises the bulk of the total. Rather than assuming an average extinction factor to estimate this

from the UV luminosity, we estimate the obscured SFR from the IR luminosity  $L_{\text{IR}}$  calculated by Reddy et al. (2006b), adopting the  $L_{\text{IR}}$ -SFR conversion factor given by Kennicutt (1998). As shown in Table 3, obscured star formation has far less compelling associations with UV morphology: none are found to have statistical significance.

The most accurate estimate of the total SFR may be found by summing the rates determined from UV and IR luminosities. We break this comparison into two cases: galaxies for which the IR-derived SFR has been directly measured using *Spitzer* MIPS detections at  $24\ \mu\text{m}$ , and galaxies that are undetected at  $24\ \mu\text{m}$  and for which an estimate of the IR-derived SFR has been computed based on the average bolometric luminosity of MIPS-undetected sources<sup>18</sup> ( $L_{\text{bol}} = 6 \times 10^{10} L_{\odot}$ ; Reddy et al. 2006b). For the first of these cases, no significant correlations are found with either the total or specific (stellar mass normalized) SFR. We note, however, that the specific SFR is on the threshold of statistical significance for a positive correlation with  $G$ . If the 11 galaxies with stellar populations younger than 40 Myr (i.e., for which stellar population fits are the most uncertain) are neglected in our analysis, this correlation becomes statistically significant, deviating from the null hypothesis by approximately  $2.1\ \sigma$ . Therefore, while there is mild evidence for a positive correlation between UV nucleation and net star formation for galaxies directly detected at  $24\ \mu\text{m}$ , this association is not at present statistically compelling. In contrast, for the  $24\ \mu\text{m}$ -undetected sources all of the associations between morphology and uncorrected UV SFR are recovered for the total estimated SFR (although this trend is smeared out by the division by mass for the specific SFR), largely because the obscured SFR extrapolated from total bolometric luminosity contributes only marginally to the total in these cases.

## 7. A COMPARISON OF MORPHOLOGIES WITH OTHER GALAXY SAMPLES

### 7.1. AGNs/QSOs

As given in the table of AGNs/QSOs in GOODS-N presented by Reddy et al. (2006a, their Table 5), there are a total of nine spectroscopically confirmed AGNs/QSOs in our sample in the redshift range  $z = 1.8\text{--}3.4$ , six of which are directly detected in X-ray emission (although one very weakly) and three of which have no X-ray counterpart to a depth of 2 Ms (based on the catalog of Alexander et al. 2003) but are confirmed AGNs based on high-ionization optical emission lines and/or power-law mid-IR SEDs. As noted by Reddy et al. (2006a), the morphologies of the X-ray-undetected sample are more disturbed than their directly detected counterparts. As we show in Figure 18, all three X-ray-undetected sources have  $G < 0.4$ , while the five detected sources all have strongly nucleated values  $G > 0.38$  (four with  $G > 0.47$ ) and the two QSOs in the sample (BMZ 1083 and MD 39) have the highest values of any object considered in this contribution at  $G = 0.63$  and  $0.88$ , respectively (close to the stellarity limit of  $G \sim 0.90$ ). This suggests a possible correlation between X-ray luminosity and UV nucleation, in the sense that AGNs that produce obvious X-ray emission also contribute sufficiently to the total UV output of their host galaxies that the centralized AGN radiation visibly affects the apparent nucleation of the UV light profile. Given the extremely small size of our sample, it is difficult to assess the global applicability of this correlation, although we note for comparison that in a larger sample of 31 AGNs in the redshift range  $z \sim 2\text{--}4$  Akiyama (2005; their Fig. 3) found that AGNs with the most centrally concentrated light distributions tended to

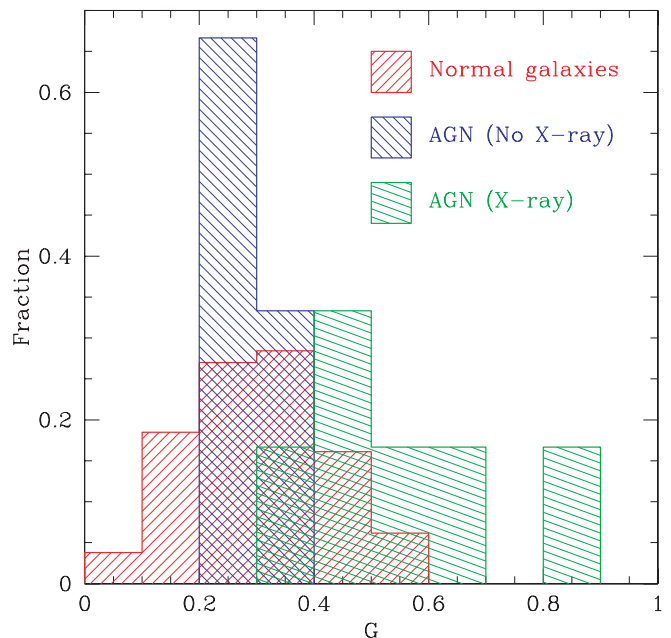


FIG. 18.—Histogram showing the relative UV nucleation for the  $z = 1.8\text{--}3.4$  galaxy sample (red histogram) versus X-ray-detected (green histogram) and X-ray-undetected AGNs/QSOs (blue histogram). The nucleation of the X-ray-undetected sample is broadly consistent with the median nucleation of the overall  $z = 1.8\text{--}3.4$  population, while X-ray-detected galaxies are more strongly nucleated.

be X-ray-bright ( $L_{2-10\ \text{keV}} > 10^{44}\ \text{ergs s}^{-1}$ ) broad-line sources, while the population of X-ray-bright narrow-line sources and X-ray-faint sources tended to be slightly less centrally concentrated. Likewise, recent studies of AGNs at lower redshifts ( $z \lesssim 1.3$ ) by Pierce et al. (2007) and Grogan et al. (2005) also found the rest-frame optical morphologies of X-ray-luminous AGNs to be more compact than those of IR-selected AGNs or ordinary field galaxies.

Not only are the X-ray-undetected AGNs more nebulous than their X-ray-bright counterparts, but we find that they also appear to have a greater number of components to their UV light, exhibiting a range of multiplicities  $\Psi = 4.6\text{--}11.8$  as compared to the  $\Psi < 1.8$  found for all directly detected X-ray sources. These irregular morphologies, coupled with a power-law SED longward of  $3\ \mu\text{m}$  (indicating the presence of warm dust) yet a UV SED well fitted by a simple stellar population, suggest (Reddy et al. 2006a) that these sources may be obscured AGNs whose UV emission is dominated by spatially extended star formation rather than a central active nucleus.

### 7.2. IR-selected BzK Galaxies

One well-studied NIR color-selected galaxy sample is the BzK-selected catalog (Daddi et al. 2004), for which many sources (52 sources brighter than  $K = 21$  in the redshift range  $z = 1.8\text{--}2.6$ ) simultaneously satisfy both the BzK selection criteria and our optical  $U_nGR$  color selection criteria. In Figure 19 we show the morphologies of those GOODS-N BzK galaxies that are comparably bright in K band and have well-determined photometric redshifts, yet fail to meet the optical selection criteria. Qualitatively, we note that the BzK galaxies not in the optically selected sample appear morphologically very similar to those in Figure 2, as might be expected given the large general overlap between the two samples and suggesting that these few galaxies may fall just outside of the optical selection criteria.

<sup>18</sup>  $L_{\text{IR}}$  effectively scales with  $L_{\text{bol}}$ .

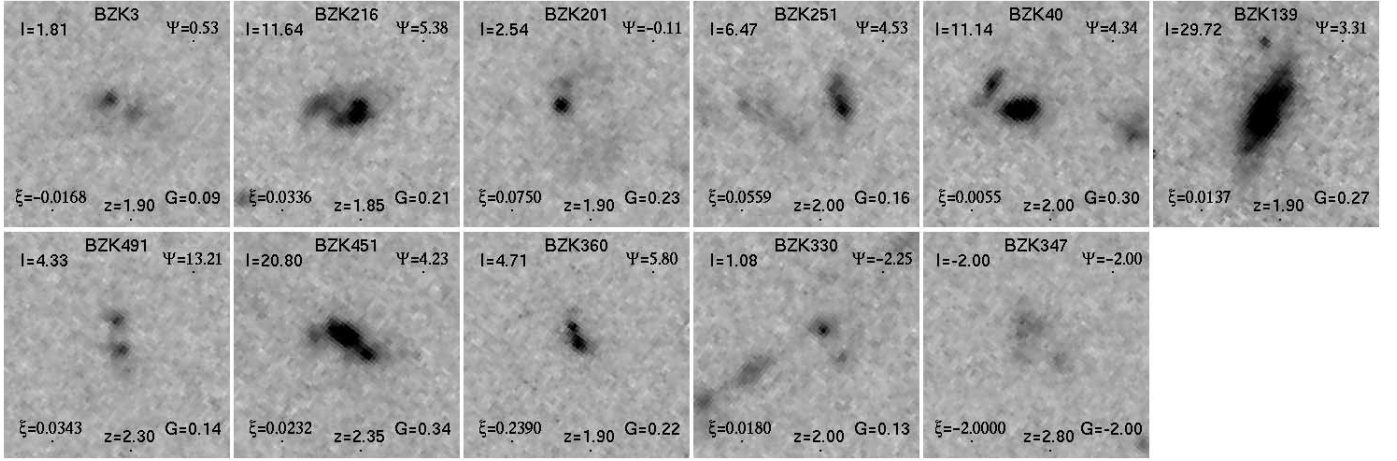


FIG. 19.—Same as Fig. 2, but for IR-selected  $BzK$  sources brighter than  $K = 21$  that are not selected by the rest-UV color selection criteria. Redshifts given are photometric.

We quantify these morphological differences in Figure 20, using photometric redshift estimates to scale the surface brightness selection algorithm. As expected based on Figure 19, the average morphology of  $BzK$  sources that are also  $U_nGR$  sources (*filled triangles*) is identical to that of the overall  $U_nGR$  sample (*filled squares*) to within the uncertainties in the mean. The sample of 11  $BzK$  sources that do *not* meet the  $U_nGR$  criteria (*open triangles*) has slightly fewer high surface brightness pixels (lower  $I$ ) and is slightly less nucleated (lower  $G$ ) than the other two samples, but at a confidence level of only 1–2  $\sigma$ . The apparent multiplicity  $\Psi$  and color dispersion  $\xi$  remain approximately constant among all of these samples to within the uncertainty.

### 7.3. IR-selected Distant Red Galaxies

Distant red galaxies (DRGs; Franx et al. 2003) constitute another major IR-selected sample of high-redshift galaxies for which there are five sources brighter than  $K = 21$  in the redshift range  $z = 1.8$ – $2.6$  that meet the  $U_nGR$  selection criteria and have secure spectroscopic redshifts, and 11 sources that do not but for which we measure reliable photometric redshifts. As illustrated by Figure 21, the DRG population is fainter and more nebulous in UV emission than any of the other galaxy samples considered, consistent with what may be expected for particularly dusty IR-bright galaxies given the apparent correlation between UV nucleation and dust extinction.

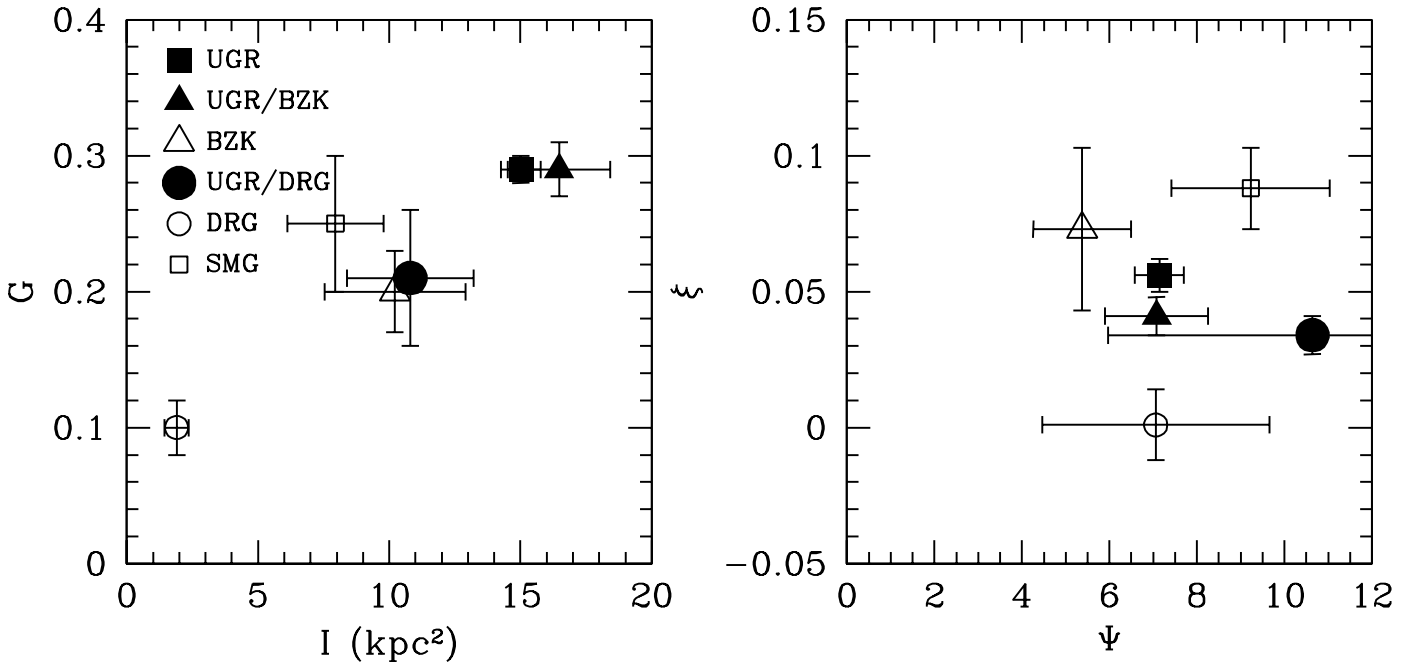


FIG. 20.—Comparative average size ( $I$ ), nucleation ( $G$ ), multiplicity ( $\Psi$ ), and color dispersion ( $\xi$ ) for optically selected  $U_nGR$ ,  $BzK$ , DRG, and SMG samples. Filled squares represent all  $z \sim 2$   $U_nGR$ -selected galaxies, filled triangles and circles the respective subsets that also fulfill  $BzK$  and DRG criteria, open triangles and circles galaxies that fulfill the  $BzK$  and DRG criteria, respectively, that do not meet the  $U_nGR$  selection criteria, and open squares all galaxies that fulfill the SMG criteria. All galaxies are limited to the redshift range  $z = 1.8$ – $2.6$  (using photometric redshifts where spectroscopic ones are unavailable), and the  $BzK$  and DRG samples are limited to those with no X-ray counterparts to 2 Ms and  $K$  magnitudes  $K < 21$ . Error bars indicate the  $1\sigma$  uncertainty in the mean values for each population.

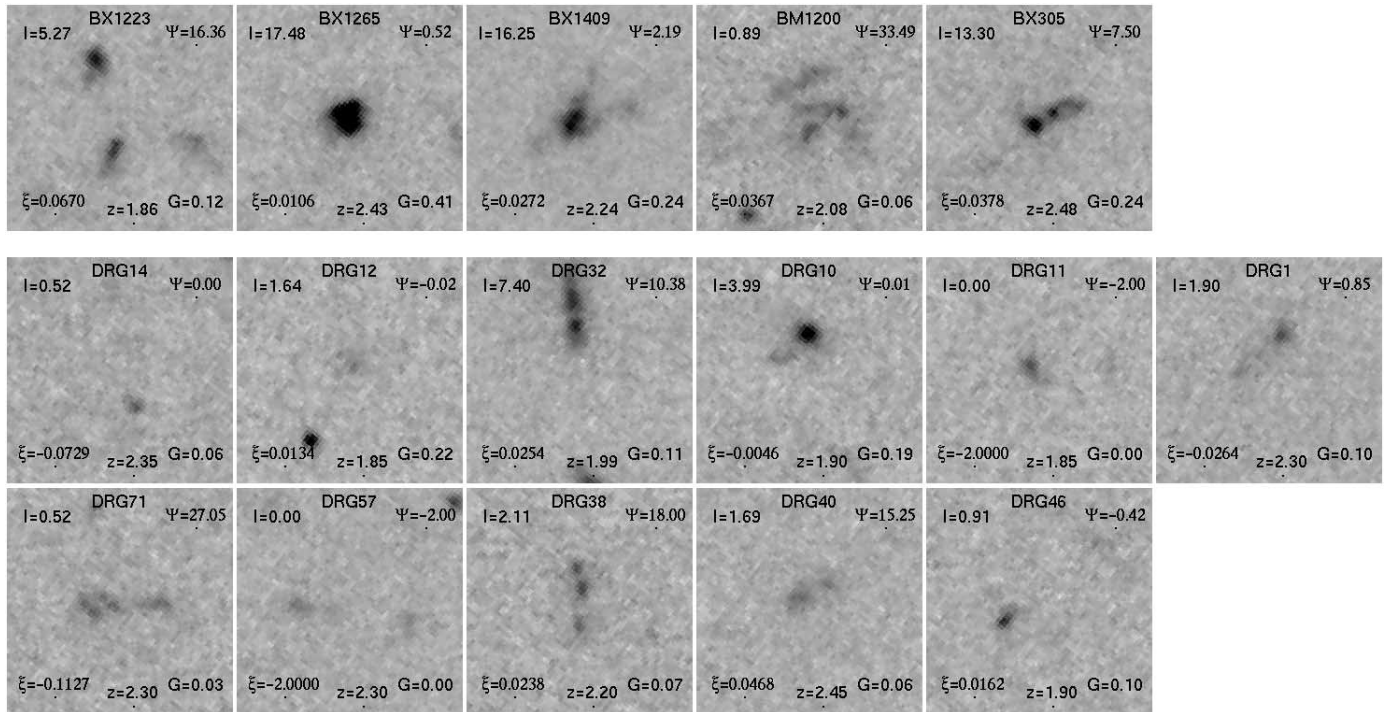


FIG. 21.—Same as Fig. 2, but for IR-selected DRG sources brighter than  $K = 21$ . *Top row*: DRGs that are also selected by rest-UV color selection criteria. *Bottom rows*: DRGs that are not selected by rest-UV color selection criteria. Redshifts given for galaxies not selected by the rest-UV criteria are photometric.

As for the *BzK* sample, the overlapping sample of  $U_nGR$ -selected DRGs has morphological coefficients similar to the bulk of the  $U_nGR$  population to within  $1-2\sigma$  (although it is on average slightly smaller and more nebulous; see Fig. 20). It is those DRGs *not* selected by  $U_nGR$  criteria, however, that particularly stand out: these galaxies (Fig. 20; *open circles*) have much smaller  $I$  and  $G$  to a high level of confidence and in some cases (e.g., DRG 14) are barely detected in our *HST* ACS imaging data. Largely, this difference is a reflection of the much fainter UV luminosity of the DRG sample: typical DRGs that do not meet the optical selection criteria have UV luminosities  $L_{1600} < 10^{10} L_{\odot}$  (and commonly  $L_{1600} < 10^9 L_{\odot}$ ), as compared to the median luminosity for the optically selected sample  $L_{1600} \sim 5 \times 10^{10} L_{\odot}$ .

Similarly to the *BzK* sample, the apparent multiplicity  $\Psi$  for DRGs is again consistent with the  $U_nGR$  sample, although the color dispersion  $\xi$  is roughly  $2\sigma$  lower and is consistent with zero (the value expected for a pure measurement of the background sky).

#### 7.4. Submillimeter Galaxies

The submillimeter galaxy (SMG) population offers the opportunity to compare the rest-UV morphologies of optically selected galaxies with those in a similar redshift range ( $z \sim 2-3$ ) that are selected on the basis of submillimeter flux. Using the catalog of SMG coordinates and spectroscopic redshifts compiled by Chapman et al. (2005), we apply our morphological analysis to

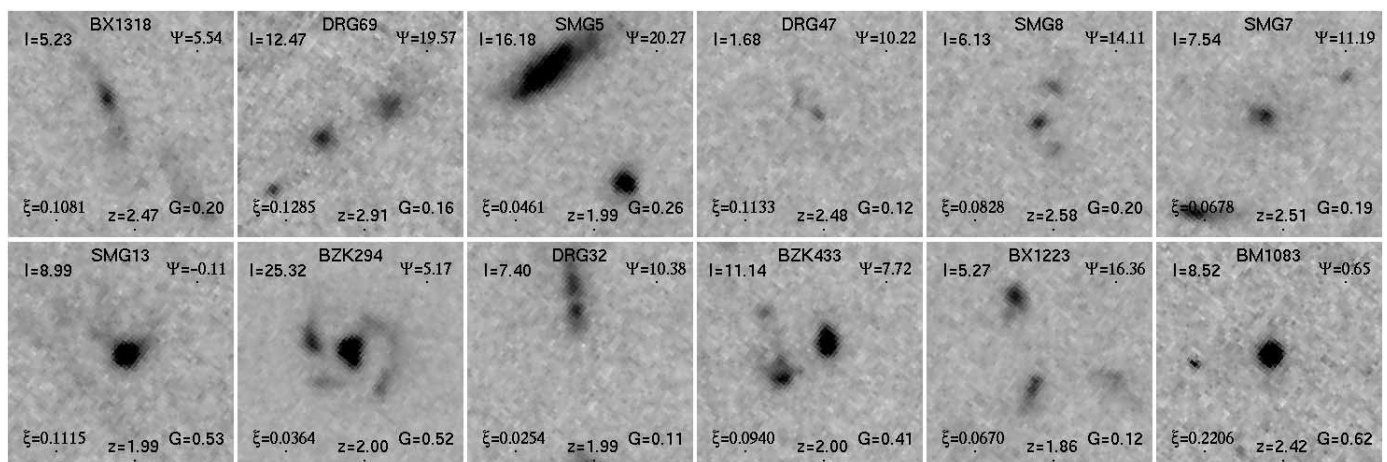


FIG. 22.—Same as Fig. 2, but for all SMGs on the *HST* ACS image frame of the GOODS-N field in the redshift range  $z = 1.8-2.6$  (plus one source at  $z = 2.91$ ). Positions and spectroscopic redshifts are drawn from the catalog of Chapman et al. (2005). Galaxies that also fulfill  $U_nGR$ , *BzK*, or DRG selection criteria are labeled accordingly. Note that the lower right object in this figure (BM 1083) is a known QSO.

a sample of these galaxies in the GOODS-N field. The wide range of morphological types covered by the SMG selection criteria are shown in Figure 22 and range from single, nucleated sources to extremely faint and nebulous and include one strong high-redshift spiral galaxy candidate (BZK 294; see Dawson et al. 2003). On average, however, the SMG population has a morphology similar to that of the  $U_nGR$ -selected sample (Fig. 20) with values of  $\Psi$  and  $\xi$  consistent to within the uncertainty and apparent sizes  $I$  and nucleations  $G$  only slightly smaller and more nebulous than the  $U_nGR$ -selected sample. These results are consistent (since our size parameter  $I$  is closely related to surface brightness) with the findings of Chapman et al. (2003) and Conselice et al. (2003b), whose *HST* STIS imaging led them to conclude that the SMG sample had lower surface brightness than typical  $z \sim 3$  LBGs, yet was slightly larger *for the reduced surface brightness*.

In addition, Conselice et al. (2003b) also find that the asymmetry index  $A$  of their sample of 11 SMGs is slightly greater on average than that of optically selected  $z \sim 3$  LBGs, which these authors conclude implies a greater major merger fraction for the submillimeter-bright sample. However, we find no statistically significant change in our multiplicity parameter  $\Psi$  (which most closely measures the morphological irregularity of a source). If the morphologies of the SMG sample are governed by the same physical processes as the optically selected galaxies (as seems likely given that the two samples appear to fall on the same trend of dustiness vs. bolometric luminosity for star-forming galaxies at  $z \sim 2$ ; Reddy et al. 2006b), then when considered nonparametrically we conclude that the SMG sample may be no more likely to be dominated by major mergers than other  $z \sim 2-3$  galaxy samples.

## 8. DISCUSSION

Through a comprehensive statistical analysis, we have found two key trends with morphology. First, the degree of nucleation/nebulosity is related to the UV/optical extinction of the source [as parameterized through both the value of  $E(B - V)$  calculated from stellar population models and the ratio of IR to UV luminosity], suggesting that more nebulous sources may appear as such since their greater quantities of dust obscure a great quantity of the UV light. Second, physically larger, more UV-luminous sources have rest-UV emission and absorption lines separated by a greater velocity, indicating that they may drive more energetic outflows than their lower luminosity counterparts. However, we note that these trends are typically on the order of  $3-4 \sigma$  significance and are far from being unambiguously convincing morphological differences. Indeed, given the relatively large sample of galaxies and volume of spectrophotometric data compiled to date, the overall *lack* of correlation between morphology and fundamental galactic properties such as stellar mass, SFR, and outflows is more remarkable. To some degree this may be due to the unknown distribution of viewing angles, but whether as a result of this complication or a more fundamental process, the rest-UV morphologies of high-redshift galaxies generally do not appear to contain a great deal of separable information. If morphologies truly mean so little, this may help explain the lack of correlation seen between elongated morphologies and major-axis velocity shear by Erb et al. (2004), who found that morphologically elongated galaxies are no more likely than compact galaxies to exhibit kinematic signatures of rotation.

It is interesting to note the implications of these findings for the major merger hypothesis, which posits that, similarly to luminous and ultraluminous infrared galaxies (LIRGs and ULIRGs) in the local universe, particularly irregular morphologies correspond

to major galaxy mergers (e.g., Conselice et al. 2003a; Chapman et al. 2003; LPM04; Lotz et al. 2006). In particular, Conselice et al. (2003a) adopt the asymmetry selection criterion  $A > 0.35$  to identify major mergers and interpret the increase in galaxy irregularity with redshift out to  $z \sim 3$  to indicate a higher merger fraction in the early universe and evidence for hierarchical formation. If the most irregular galaxies truly represent such major events, however, we might reasonably expect these galaxies to differ significantly from their nonmerging counterparts in some additional way, perhaps by displaying tidally enhanced rates of star formation or broadened interstellar absorption lines due to the juxtaposition of the ISM of two or more galaxies with relative velocity differences of order a few hundred kilometers per second. However, we find no evidence for such a distinction between any of a variety of morphological samples, suggesting either that major mergers at  $z \sim 2-3$  are largely indistinguishable from the nonmerging sample, that *all*  $z \sim 2-3$  galaxies are experiencing major merger-induced starbursts, or simply that irregular morphology (at least to within  $\sim 13$  kpc at rest-UV wavelengths) is not a reliable indicator of a major merger. While it is possible that major mergers may be distinguishable on the basis of multiple components beyond our 13 kpc detection threshold, it seems unlikely that such systems would produce changes as profound as may be found on closer passes.

Supposing then that irregular, multicomponent morphologies do *not* represent bursts of star formation in the orbiting galaxies and satellite galaxies of a major merger, another possibility is that these systems may instead represent patchy star formation occurring from the collapse of local instabilities within galactic molecular clouds. Combined with the complicating effects of dust and viewing angle, such an explanation may fit the local LBG analog VV 114, based on the UV and NIR imaging of Goldader et al. (2002). It is also possible that, in some small number of cases, multicomponent morphologies may reflect objects that are nearby in projection, but unrelated due to large differences in redshift. While individual components of multicomponent objects have not been spectroscopically confirmed to be associated, however, the angular distribution of sources suggests that such projection effects should contribute minimally to the total population.

Finally, we note that while the rest-UV and rest-optical morphologies of  $z \sim 2-3$  galaxies are similar in the majority of cases (as shown by Dickinson 2000) and appear to contain little separable information, there is a small subsample of these galaxies for which the optical morphologies appear considerably more regular and “evolved” than their UV counterparts (Toft et al. 2005). It may be the case that this small population of galaxies has rest-optical morphologies that are easier to interpret than the majority of the galaxy sample and may have useful correlations between rest-optical morphology and spectrophotometric or kinematic indices. In particular, such galaxies are intriguing possible targets for future kinematic study with the aid of AO-assisted integral field spectroscopy (e.g., Förster-Schreiber et al. 2006; Law et al. 2006), which could demonstrate whether these galaxies are any more likely than the rest of the galaxy sample to contain tractable meaning in their luminous spatial structures.

D. R. L. and C. C. S. have been supported by grant AST 03-07263 from the US National Science Foundation and archival grant HST-AR 10311 from the Space Telescope Science Institute. The authors thank Rupali Chandar and Christy Tremonti for helpful communications.

## REFERENCES

- Abraham, R. G., Tanvir, N. R., Santiago, B. X., Ellis, R. S., Glazebrook, K., & van den Bergh, S. 1996, *MNRAS*, 279, L47
- Abraham, R. G., van den Bergh, S., & Nair, P. 2003, *ApJ*, 588, 218
- Adelberger, K. L., Shapley, A. E., Steidel, C. C., Pettini, M., Erb, D. K., & Reddy, N. A. 2005, *ApJ*, 629, 636
- Adelberger, K. L., Steidel, C. C., Shapley, A. E., Hunt, M. P., Erb, D. K., Reddy, N. A., & Pettini, M. 2004, *ApJ*, 607, 226
- Akiyama, M. 2005, *ApJ*, 629, 72
- Alexander, D. M., et al. 2003, *AJ*, 126, 539
- Bershady, M. A., Jangren, A., & Conselice, C. J. 2000, *AJ*, 119, 2645
- Chandar, R., Leitherer, C., Tremonti, C. A., Calzetti, D., Aloisi, A., Meurer, G. R., & de Mello, D. 2005, *ApJ*, 628, 210
- Chapman, S. C., Blain, A. W., Smail, I., & Ivison, R. J. 2005, *ApJ*, 622, 772
- Chapman, S. C., Windhorst, R., Odewahn, S., Yan, H., & Conselice, C. 2003, *ApJ*, 599, 92
- Conselice, C. J. 2003, *ApJS*, 147, 1
- Conselice, C. J., Bershady, M. A., Dickinson, M., & Papovich, C. 2003a, *AJ*, 126, 1183
- Conselice, C. J., Bershady, M. A., & Jangren, A. 2000, *ApJ*, 529, 886
- Conselice, C. J., Blackburne, J. A., & Papovich, C. 2005, *ApJ*, 620, 564
- Conselice, C. J., Chapman, S. C., & Windhorst, R. A. 2003b, *ApJ*, 596, L5
- Daddi, E., Cimatti, A., Renzini, A., Fontana, A., Mignoli, M., Pozzetti, L., Tozzi, P., & Zamorani, G. 2004, *ApJ*, 617, 746
- Dawson, S., McCrady, N., Stern, D., Eckart, M. E., Spinrad, H., Liu, M. C., & Graham, J. R. 2003, *AJ*, 125, 1236
- Dickinson, M. 2000, *Philos. Trans. R. Soc. London A*, 358, 2001
- Dickinson, M., Papovich, C., Ferguson, H. C., & Budavári, T. 2003, *ApJ*, 587, 25
- Erb, D. K., Shapley, A. E., Pettini, M., Steidel, C. C., Reddy, N. A., & Adelberger, K. L. 2006a, *ApJ*, 644, 813
- Erb, D. K., Steidel, C. C., Shapley, A. E., Pettini, M., & Adelberger, K. L. 2004, *ApJ*, 612, 122
- Erb, D. K., Steidel, C. C., Shapley, A. E., Pettini, M., Reddy, N. A., & Adelberger, K. L. 2006b, *ApJ*, 646, 107
- Ferguson, H. C., et al. 2004, *ApJ*, 600, L107
- Förster Schreiber, N. M., et al. 2006, *ApJ*, 645, 1062
- Franx, M., et al. 2003, *ApJ*, 587, L79
- Giavalisco, M., et al. 2004, *ApJ*, 600, L93
- Gini, C. 1912, reprinted in *Memorie di Metodologia Statistica*, ed. E. Pizetti & T. Salvemini (1955; Rome: Libreria Eredi Virgilio Veschi)
- Glasser, G. J. 1962, *J. Am. Stat. Assoc.*, 57, 648
- Goldader, J. D., Meurer, G., Heckman, T. M., Seibert, M., Sanders, D. B., Calzetti, D., & Steidel, C. C. 2002, *ApJ*, 568, 651
- Gordon, K. D., et al. 2004, *ApJS*, 154, 215
- Grimes, J. P., Heckman, T., Hoopes, C., Strickland, D., Aloisi, A., Meurer, G., & Ptak, A. 2006, *ApJ*, 648, 310
- Grogin, N. A., et al. 2005, *ApJ*, 627, L97
- Kajisawa, M., & Yamada, T. 2001, *PASJ*, 53, 833
- Kennicutt, R. C., Jr. 1998, *ARA&A*, 36, 189
- Kent, S. M. 1985, *ApJS*, 59, 115
- Law, D. R., Steidel, C. C., & Erb, D. K. 2006, *AJ*, 131, 70
- Lotz, J. M., Madau, P., Giavalisco, M., Primack, J., & Ferguson, H. C. 2006, *ApJ*, 636, 592
- Lotz, J. M., Primack, J., & Madau, P. 2004, *AJ*, 128, 163 (LPM04)
- Papovich, C., Dickinson, M., Giavalisco, M., Conselice, C. J., & Ferguson, H. C. 2005, *ApJ*, 631, 101
- Papovich, C., Giavalisco, M., Dickinson, M., Conselice, C. J., & Ferguson, H. C. 2003, *ApJ*, 598, 827
- Petrosian, V. 1976, *ApJ*, 209, L1
- Pettini, M., & Pagel, B. E. J. 2004, *MNRAS*, 348, L59
- Pettini, M., Rix, S. A., Steidel, C. C., Adelberger, K. L., Hunt, M. P., & Shapley, A. E. 2002, *ApJ*, 569, 742
- Pierce, C. M., et al. 2007, *ApJ*, in press (astro-ph/0608381)
- Ravindranath, S., et al. 2006, *ApJ*, 652, 963
- Reddy, N. A., Steidel, C. C., Erb, D. K., Shapley, A. E., & Pettini, M. 2006a, *ApJ*, 653, 1004
- Reddy, N. A., Steidel, C. C., Fadda, D., Yan, L., Pettini, M., Shapley, A. E., Erb, D. K., & Adelberger, K. L. 2006b, *ApJ*, 644, 792
- Rix, S. A., Pettini, M., Leitherer, C., Bresolin, F., Kudritzki, R.-P., & Steidel, C. C. 2004, *ApJ*, 615, 98
- Schade, D., Lilly, S. J., Crampton, D., Hammer, F., Le Fevre, O., & Tresse, L. 1995, *ApJ*, 451, L1
- Shapley, A. E., Steidel, C. C., Erb, D. K., Reddy, N. A., Adelberger, K. L., Pettini, M., Barnby, P., & Huang, J. 2005, *ApJ*, 626, 698
- Shapley, A. E., Steidel, C. C., Pettini, M., & Adelberger, K. L. 2003, *ApJ*, 588, 65
- Steidel, C. C., Adelberger, K. L., Shapley, A. E., Pettini, M., Dickinson, M., & Giavalisco, M. 2003, *ApJ*, 592, 728
- Steidel, C. C., Shapley, A. E., Pettini, M., Adelberger, K. L., Erb, D. K., Reddy, N. A., & Hunt, M. P. 2004, *ApJ*, 604, 534
- Toft, S., van Dokkum, P., Franx, M., Thompson, R. I., Illingworth, G. D., Bouwens, R. J., & Kriek, M. 2005, *ApJ*, 624, L9